DESIGN OF A MEMS BASED HYDRAULIC PRESSURE SENSOR

A THESIS SUBMITTED TO
THE GRADUATE SCHOOL OF NATURAL AND APPLIED SCIENCES
OF
MIDDLE EAST TECHNICAL UNIVERSITY

BY

UTKU GÖREKE

IN PARTIAL FULFILLMENT OF THE REQUIREMENTS
FOR
THE DEGREE OF MASTER OF SCIENCE
IN
MICRO AND NANOTECHNOLOGY

FEBRUARY 2016

Approval of the thesis:

DESIGN OF A MEMS BASED HYDRAULIC PRESSURE SENSOR

submitted by **UTKU GÖREKE** in partial fulfilment of the requirements for the degree of **Master of Science in Micro and Nanotechnology Department, Middle East Technical University** by,

Prof. Dr. Gülbin Dural Ünver ________________
Dean, Graduate School of **Natural and Applied Sciences**

Prof. Dr. Tayfun Akın ________________
Head of Department, **Micro and Nanotechnology**

Assist. Prof. Dr. Kıvanç Azgın ________________
Supervisor, **Micro and Nanotechnology, METU**

Assist. Prof. Dr. Mustafa Ilker Beyaz ________________
Co-supervisor, **Electrical and Electronical Eng. Dept., Int. Ant. Uni.**

Examining Committee Members:

Prof. Dr. Mehmet Çalışkan ________________
Mechanical Eng. Dept., METU

Assist. Prof. Dr. Kıvanç Azgın ________________
Micro and Nanotechnology., METU

Prof. Dr. Haluk Külah ________________
Electrical and Electronics Eng. Dept., METU

Assist. Prof. Dr. Mustafa Ilker Beyaz ________________
Electrical and Electronical Eng. Dept., Int. Ant. Uni

Assist. Prof. Dr. Ali Emre Turgut ________________
Mechanical Eng. Dept., METU

I hereby declare that all information in this document has been obtained and presented in accordance with academic rules and ethical conduct. I also declare that, as required by the rules and conduct, I have fully cited and referenced all materials and results that are not original to this work.

Utku Göreke

ABSTRACT

DESIGN OF A MEMS BASED HYDRAULIC PRESSURE SENSOR

Göreke, Utku

M.S., Department of Micro and Nanotechnology Department

Supervisor : Assist. Prof. Dr. Kıvanç Azgın

Co-Supervisor : Assist. Prof. Dr. Mustafa Ilker Beyaz

February 2016, 85 pages

This dissertation presents a novel technique for detection of hydraulic pressure by using a MEMS resonant sensor. Proposed sensor utilizes a double ended tuning fork (DETF) resonator. In the literature tuning forks are used for measurement of the deflection of a diaphragm. However, in this study, a tuning fork is configured to lay in orthogonal direction with a diaphragm of which center point deflection is being measured. Upon application of pressure, center deflection of the diaphragm induces an axial compressive load on the DETF resonator which induces decrease in natural frequency of the resonator. Since the tip is vulnerable, a roller structure which is simply a guided beam is included in the design to protect tip from transverse components of measured displacement. Additionally, the applied displacement is directed through the roller to a spring element which transmits nearly 1 % of tip displacement to DETF. Although the addition of the spring adversely affects the sensitivity, the spring increases the overall compliance of the tip which increases the assembly yield. Advantage of such design is that by modifying the geometry of the spring or the diaphragm, different pressure ranges for measurement can be attained. The resonator's tine dimensions are optimized for maximum of sensitivity quality factor product. The device can operate in atmospheric conditions, and hence the design makes use of overlapping comb fingers to avoid squeeze film damping.

A pressure port is designed to keep diaphragm and MEMS sensor together in contact. The pressure port combines the deflection performance of aluminum for better sensitivity, and greater strength of steel for larger safety factor. Aluminum and steel parts are fixed together with interference fit for demonstration of the sensor operation.

Surface micromachining of MEMS sensor is carried out at METU-MEMS cleanroom facility. Process flow involves 3 photolithography steps and makes use of 1 silicon-on-insulator (SOI) wafer. Pressure port is manufactured with conventional machining.

Operation principle and analytical model is validated with FEM simulations. Tests are conducted for both tip displacement for sensor core and hydraulic pressure for the overall assembly. Resonator quality factor and maximum sensitivity measured in tip displacement tests were 238 and 198.49 Hz/μm, respectively, which is equivalent of 9.45 Hz/Bar with an aluminum diaphragm with 6.2 mm diameter and 1 mm thickness. A maximum sensitivity of 34.40 is achieved in hydraulic pressure tests.

As a summary, operation of tuning fork resonator in orthogonal configuration with a diaphragm as a hydraulic pressure sensor is demonstrated. Proposed novel configuration promises a high dynamic range hydraulic pressure measurement.

Keywords: Double Ended Tuning Fork, Resonator, Hydraulic, Pressure, Sensor, Design Optimization, Atmospheric Operation, Surface Micromachining, MEMS

ÖZ

MEMS TABANLI HİDROLİK BASINÇ SENSÖRÜ TASARIMI

Göreke, Utku

Yüksek Lisans, Mikro ve Nanoteknoloji Bölümü
Tez Yöneticisi : Yar. Doç. Dr. Kıvanç Azgın
Ortak Tez Yöneticisi : Yar. Doç. Dr. Mustafa Ilker Beyaz

Şubat 2016, 85 sayfa

Bu tez mikroelektromekanik sistem (MEMS) rezonatör kullanarak hidrolik basınç algılanması için özgün bir teknik sunmaktadır. Önerilen algılayıcı, bir çift taraflı ayarlama çatalı rezonatöründen faydalanmaktadır. Ayarlama çatalı, literatürde bir diyaframın esnemesini ölçmek için kullanılmıştır. Ancak, bu çalışmada ayarlama çatalı, orta noktasındaki esneme miktarı ölçülecek olan diyafram ile dik şekilde konumlandırılmıştır. Hidrolik basınç uygulandığında diyafram orta noktasında oluşan esneme, rezonatör üzerinde eksenel sıkıştırıcı yönde gerginlik üretmekte ve bu gerginlik doğal frekansın azalma yönünde kaymasına neden olmaktadır. Ayarlama çatalının ucu kolayca zarar görebileceği için, tasarıma, ucu ölçülen yer değiştirmenin eksene dik bileşenlerinden korumak için, kayıcı mesnet yapısı eklenmiştir. Ayrıca, kayıcı mesnet tarafından yönledirilen yer değiştime, uç yer değiştirmesinin yaklşık % 1’ ini çift taraflı ayar çatalına aktaran bir yay yapısı üzerinden geçerek çift taraflı ayarlama çatalına ulaşmaktadır. Yayın

eklenmesi hassasiyeti olumsuz yönde etkilese de, yay, ucun esnekliğini artırarak montaj verimini artırmaktadır. Bu tasarımın yararı, yay veya diyafram geometrisi üzerinde değişiklik yapılarak farklı basınç aralıkları için ölçüm gerçekleştirilebilmesine izin vermesidir. Rezonatör çatalının ölçüleri, hassasiyet ve kalite etkeninin en büyük bileşkesini elde etmek üzere en iyilenmiştir. Algılayıcı, atmosfer basıncı altında çalışabilmektedir ve bu yüzden tasarım, sıkışan film sönümlemesinin etkisinden kaçınmak için örtüşen tarak parmaklarından yararlanmaktır.

MEMS rezonatör ve diyaframı bağlantı halinde tutmak için bir basınç bağlantı yapısı tasarlanmıştır. Bu basınç bağlntı yapısı, daha yüksek hassasiyet için alüminyumun daha üstün esneme kabiliyetini, daha yüksek güvenlik katsayısı için çeliğin çekme mukaveti üstünlüğü ile birleştirmektedir. Alüminyum ve çelik parçalar algılayıcının çalışmasını göstermek için sıkı geçme ile geçirilerek sabitlenmiştir.

MEMS algılayıcı, silisyum mikroişleme ile ODTÜ-MEMS Merkezi' nin temizalanında üretilmiştir. Süreç akımı, 3 tane fotolitografi adımından içermekte ve 1 adet SOI (yalıtkan üzerinde silisyum) pul kullanmaktadır.

Çalışma prensibi ve analitik model sonlu eleman analizi simulasyonları ile doğrulanmıştır. Sensör çekirdeği üzerinde uç yer değiştirmesi testleri, tüm cihaz üzerinde de hidrolik basınç testleri gerçekleştirilmiştir. Yer değiştime testlerinde rezonatör kalite faktörü ve en yüksek hassasiyet değerleri sırasıyla 238 ve 198.49 Hz/Bar olarak ölçülmüştür. Bu yer değiştirme hassasiyetinin basınç hassasiyeti karşılığı, 1 mm kalınlığında ve 6.2 mm çapında alüminyum diyafram için 9.45 Hz/Bar olarak hesaplanmaktadır. Hidrolik basınç testlerinde en yüksek hassasiyet değeri 33.40 Hz/Bar olarak ölçülmüştür.

Sonuç olarak, ayarlama çatalı rezonatörünün, diyaframa dik konumda hidrolik basınç sensörü olarak kullanılması gösterilmiştir. Önerilen bu özgün konumlama, yüksek dinamik aralık vaadetmektedir.

Anahtar Kelimeler: Çift Taraflı Ayarlama Çatalı, Rezonatör, Hidrolik, Basınç, Sensör, Tasarım Eniyilemesi, Atmosfer Ortamında Çalışma, Silisyum Mikroişleme, Mikroelektromekanik Sistemler (MEMS)

To my family,

ACKNOWLEDGEMENTS

I would like to express my gratitude to my advisor Dr. Kıvanç Azgın for his guidance, comments. He created a very friendly relationship with me and always let me experience practical subjects beyond books. Also I would like to thank to my co-advisor Dr. Mustafa İlker Beyaz who always gave precious feedbacks through this study and for his caring attitude. I'm also grateful to him for supporting me financially through my research.

I would like to thank to all METU-MEMS members individually for the nice atmosphere inside and outside of laboratory. Especially, Akın Aydemir, Eyüp Can Demir and Taylan Töral shared their valuable time for this work and I gained lots of experience with them.

Very special thanks goes to Talha Köse for his valuable friendship, discussions, and help on cleamroom fabrication. He is such a good guy. Also I would have very trouble time without Ulaş Aykutlu and Yunus Terzioğlu in tests. I would like to express my appreciation for their precise and priceless work. They gave what money cannot buy. Also Mecid Uğur Dilberoğlu and Sedat Pala assisted me a lot and their support was very valuable. I would like to thank them for their kind and helpful attitude, these guys are rare. Also thanks to my lab friends for not leaving me alone.

I feel like I have to express the names of my friends individually while acknowledging their support. Thank you, Can Ekmekçi, Ahmet Ademoğlu, Özenç Güngör, Batu Aksu, Fatih Küçüksubaşı, Berkman Kantar, Serkan Ülgen, Family Vural, Family Bayram, Family Çelik, Ahmet Yıldırım, Dilara Gündoğdu, Volkan Aksu, Sırma Örgüç, Gülşah Demirhan, Arda Akay, Anıl Alan and Can Baloğlu. You are great!

Lastly, I would like to thank to my family for their endless help, support and encouragement and trust. My gratitude to them is eternal.

TABLE OF CONTENTS

LIST OF TABLES

TABLES

LIST OF FIGURES

FIGURES

CHAPTER 1

INTRODUCTION

Technology of miniature devices have advanced enormously especially in the last two decades, becoming widespread tools of the new epoch for humankind. In this period of past, it became possible to reach out vast amount of information about the universe with little effort. New drones are sent to deep space to collect, while we also have little knowledge about the Earth. Nobody tries to land on the moon anymore but some have thoughts about mining it. Information is endless yet gathering it, is difficult and slow therefore it is what defines the pace of us. Herein an important aspect to take into account is that information is either acquired or verified by experiments and measurements. Actually this is the main reason why miniature devices are so common and changed our perception of life at present, they are superior measurement tools.

Among those miniature devices, MEMS devices are the most popular ones for the time being. They are present actually everywhere functioning, sensing, actuating. As a very common example of sensory applications clocks can be given. Although quartz is an excellent tool for measuring time, most of the clocks are using MEMS resonators instead of quartz today due to extreme low cost and ease of fabrication.

Since 1982, the year when silicon is proposed as a mechanical material [1], silicon and hence MEMS are available in devices ranging from clocks to satellite propulsion [2]. Although, subjects such as micro scale phenomena and use of silicon as a material are investigated thoroughly, there are still lots of available experiments in which information is waiting to be unearthed.

In this study measurement of pressure relies on use of diaphragm and strain sensor similar to many other publications. But this dissertation offers a novel. Being distinct from other studies, diaphragm and resonator is not in parallel position. Instead, resonator is positioned orthogonally with respect to diaphragm. By using this property design can achieve higher resolution in a broader range. Moreover this property enables design to work with different diaphragm geometries without modifying the MEMS component.

1.1. Dissertation Outline

The outline of the dissertation starts with brief introductory part in the first chapter of which aim is to express motivation through basics of the design, possible areas of application and literature review of pertaining studies. Then in the second chapter, the theory behind the design process is explained. Objective of this part is to explain how this design will be brought to life. Therefore frequency shift phenomenon for a tuning fork structure is unfolded first. Then, quality factor estimation, one of the important aspects while deciding on the design, is interpreted. The third chapter relies heavily on subtask of double ended tuning fork (DETF) optimization of the design. But it also includes design of pressure port and other supplementary structures. Purpose of the third chapter is to combine the knowledge with analysis in detail. After that in the fourth chapter, fabrication of sensor core and pressure port is explained. In the fifth chapter, characterization of the devices is covered and results are pointed out. Lastly in the future remarks and discussions chapter, the outputs of the study are wrapped up and the final comments are made.

1.2. Design Basics of the Hydraulic Pressure Sensor

One advantage of design is that it makes use of a DETF resonator. These type of resonators have excellent mechanical properties. They can operate in the presence of parasitic elements without their mechanical properties being affected. Also they have very low hysteresis [3]. These two properties yields high stability for DETF but moreover, it does not require a large proof mass and this boosts sensitivity to a superior level.

Since the design is a fusion of two parts, namely pressure port and MEMS resonator, it offers high dynamic range of operation. More specifically, it is possible to change the pressure port element while keeping the resonator part the same, in order to achieve greater pressure limits. It should be noted that, in this study, pressure sensor is tested under maximum pressure of 60 bars. When this pressure is converted to displacement via diaphragm of the design, it is well below 10 µm. Yet, DETF is designed to endure 100 µm of axial compression without buckling with a set of spring elements. Therefore resonator part can easily accompany more complex pressure port types which can endure higher pressure applications.

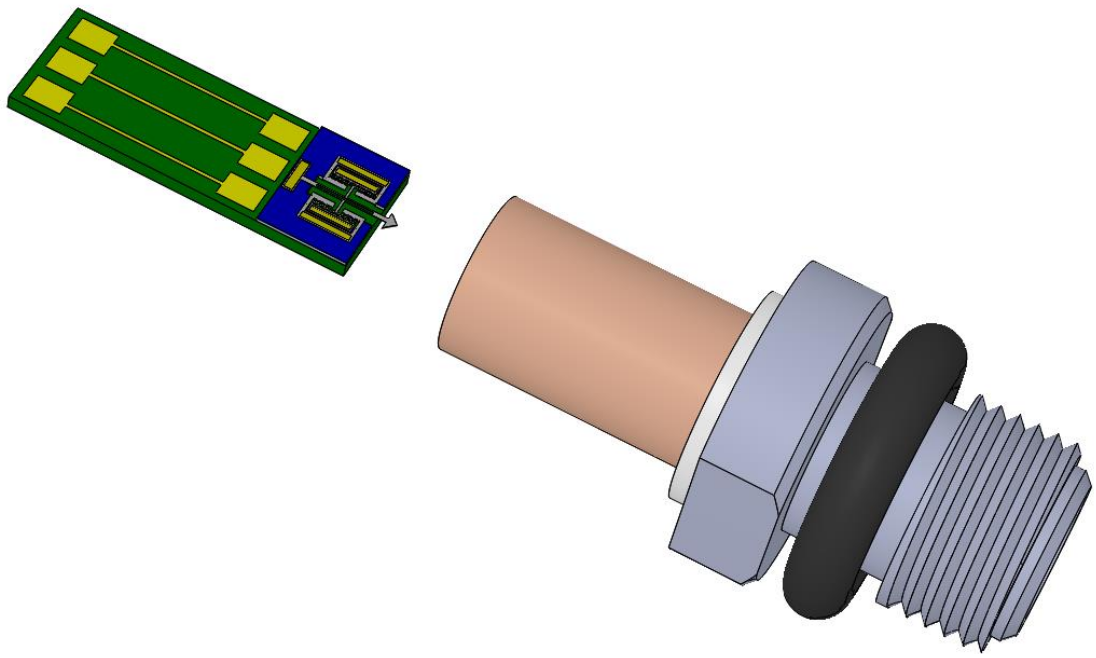

Figure 1.1 - Complete view of sensory part on the left and pressure port part on the right

It is necessary for resonator tip and diaphragm to be in physical contact. Therefore assembling the parts of the sensor is a critical step in which DETF is under risk of damage. The most important objective of setting axial compression limit to a large value is to secure the DETF structure from shocks. Due to high axial compression limit, faults which may occur while assembling the parts of the structure are less likely to be able to inflict harm. Thus robustness of the sensor is increased.

Another important specification of proposed sensor is that it can operate under atmospheric pressure while attaining sufficiently high quality factor values. Normally operation in vacuum is desired scenario for MEMS resonators. This is because air between the gaps of micro structure dissipates energy and also may act as a spring. As a consequence, quality factor of the structure degrades which in turn means, less sensitivity and more input power to drive the system at resonance. But operation in vacuum brings certain burden on the fabrication and testing of the devices. And particularly, it is difficult to sustain package level vacuum for such strain sensing element which needs to interact the outer world mechanically with its tip. Therefore in order to achieve high quality values while operating under atmospheric conditions, dissipative factors which act as a damper to the system is explored well and design is shaped as needed.

A printed circuit board is employed as a mid-step for electrical connections. Board's one end is reserved for mounting resonator and the other part is used for taking the cables out. The electrical connections of the resonator part are made via wire bonder while cables are soldered. There is a void distance on the board between two sets of pads which decreases the risk of getting MEMS device with close contact to boiling solder material.

1.3. Areas of Application

Proposed sensor design has an objective of sensing high hydraulic pressures. This is provided with the large maximum deflection limit of the resonator, dynamically. Variety of application areas which requires high hydraulic pressure is available in industry. In this section brief information will be given about these areas and the way that presented sensor can be utilized.

Demand for high hydraulic pressure is highly related with manufacturing industry and hydroforming of ductile metals is one of the main applications. In this manufacturing approach sheet of metal is fed to a die. Then hydraulic fluid is pumped into the chamber where metal will form. The importance of measuring internal pressure is due to process parameters, because outside a certain interval failures such as wrinkles may be observed [4]. Moreover on top of die forming, drawing techniques are currently used via hydroforming. This technique also depends on the pressure of the fluid because the drawing rate of the metal which is an important factor of successful operation is pressure dependent [5].

Bolt tensioning is another high hydraulic pressure process employed by industry. In this technique bolting area is squeezed with hydraulic pressure in order to attain certain bolting pre-stress. Then bolt is rotated easily to clamp two squeezed materials together. Tensioning a bolt hydraulically yields better precision and hydraulic pressure is directly related with the amount of tension for this method. And hence it is directly related with precision that method promotes.

Natural disaster warning systems are one of the interesting application area of the sensor. Actually specification requirements of these systems are never fully satisfied before. Recently, a sensor type which resembles to proposed design of dissertation is named as breakthrough for its resolution [6]. Related design will be discussed in detail literature review section but it is important to state that these warning systems are in hunger for better pressure resolutions. In corresponding study, few sensors, one of which is a hydraulic pressure sensor, are sent into surface of ocean. Below 6000 meters of the sea level which corresponds to approximately 600 bars, measurement of above hydraulic pressure takes place. High pressure resolution facilitates discrimination of earthquakes from a tsunami. Before the publication of the study few distant tsunamis are monitored. After that time these sensors are utilized in DONET research in Japan [7].

High pressure processing (HPP) is yet another application of such sensor. Very similar to ultra-high temperature (UHT) treatment, foods can be freed from septic. In these applications hydrostatic pressures as high as 4000 bars are required [8].

High pressures such as 1000 bars are also used commonly in autofrettage technique of which is used for increasing fatigue life of tube components [9]. This is a commonly used method in automotive industry for fuel injection systems. In this method, pressure is applied to the inner wall of tube, creating a compressive stress on the inner wall. This residual pressure helps engineers to increase fatigue life without increasing outer diameter and wasting more material.

1.4. Literature Review

In this section resonant pressure sensors are reviewed in detail first. Then example sensor applications of DETF resonators are investigated.

1.4.1. Resonant Pressure Sensors

Pressure sensors are found in variety of structural forms, detection and actuation methods for variety of ranges and applications. For example optically driven MEMS pressure sensor is reported with a broad range [10] and it is an application specific design of which objective is to endure harsh conditions while taking single point pressure measurements out of a fiber cable. Although it has a wide measurement range, 0 – 206 bars, and proposes minimal linear drift, 250 ppm, it lacks in sensitivity, 0.13 Hz/kPa. There are highly sensitive solutions as well, such as presented by Fragiacomo [11], a touch mode capacitive pressure sensor. It is nominated that presented sensor has the highest sensitivity of its kind as 14 pF/bar. But according to authors it has disadvantages such as hysteresis, process reliability problems and complex conditioning electronics. Also it lacks for its full scale being between 0-10 bars. Furthermore, there are lots of available piezoresistive pressure sensors available in the market due to their low costs. They are highly compatible with integrated circuits processes and obtained through series of basic cleanroom processes [11]. In addition to that, excellent linearity is served by piezoresistors [12, 13]. But disadvantages are inevitable temperature drift [14] and insufficient sensitivity for this efficient option [15].

On the other hand resonators have several of advantages over most commonly approved capacitive and piezoresistive counterparts. Their output can easily be acquired and digitized event with cheap frequency counters and, they can be combined with detection electronics with little effort [16]. Moreover resonators natural frequency is only effected by its geometry and mechanical properties other than temperature therefore electrical noise and drift is an insignificant concern for resonators [17]. This brings long term stability as an advantage in comparison with the other techniques. In addition to that, resonators are superior in terms of sensitivity [18]. One disadvantage of silicon resonators is that they can be easily degraded due to poor packaging conditions and other residual stress pertaining to fabrication [19]. Nevertheless, proposed design of dissertation neither requires any packaging nor has a complicated and stress resulting fabrication step. Therefore resonators suit well with the operation and seem like the best candidate.

There are numerous resonator devices used for measuring pressure in the literature. Most of these devices have resonators in parallel position with the diaphragm. Ren and Welham have reported very simple examples of such designs which resemble to each other [20, 21]. Corresponding tuning forks of two studies are shown in Figure 1.2. Both of the studies have utilized comb finger for drive and sense electrodes and have close natural frequency values as 35 and 52 kHz, respectively.

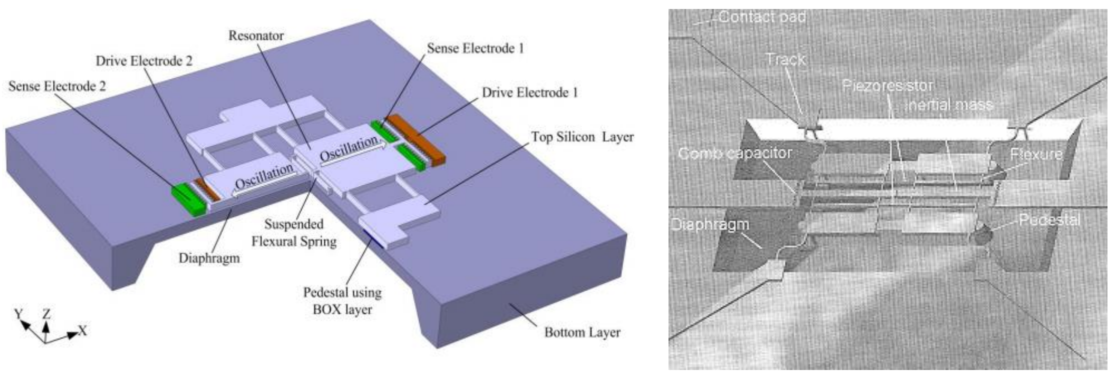

(a) (b)

Figure 1.2 - Illustrative view of two similar simple methods adopted by early researchers. (a) Fabrication view of DETF on a daiphragm from [20] and (b) fabricated view from [21]

Intentions of both studies were to run devices under atmospheric conditions and hence reported quality factors of two studies are around 1000. Measurements are taken in an interval of 0-6 and 0-10 bars, respectively. These two publications shows one of the simplest ways of measuring pressure with a resonator. Another approach two mentioned designs is presented by driving the resonator to its resonance electromagnetically instead of using comb fingers and electrostatic method [22]. Compared with the former ones, this research reports 0-1 bar range with 10 Pa resolution. The sensitivity of the device is around 6 times higher than the previous studies, being 122 kHz/Pa.

Bo suggested using a similar design which tuning forks are used, but under vacuum [23]. Bo's design which is shown in Figure 1.3, made use of wafer level packaging and also utilized capacitive plates for sense and drive electrodes instead of comb fingers because squeeze film damping is not a concern for devices running in vacuum conditions. As a consequence this research achieved higher quality factors of around 10000 after 6 months of operation. Yet the sensitivity reported is close to previous researches, being 166 Hz/kPa.

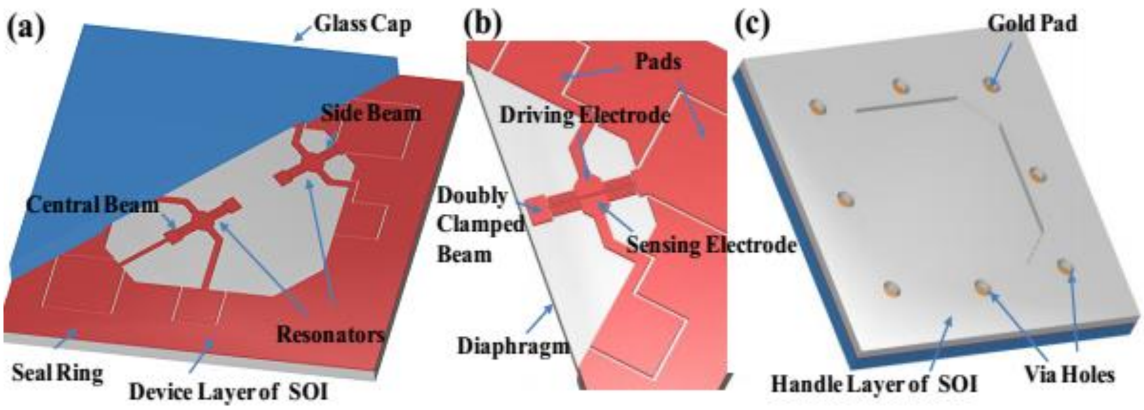

Figure 1.3 - Cross sectional and packaged view of a wafer level vacuum packaged pressure sensor [23]

A study published in 2009 by Kinnell, reports a design which is designed to operate under vacuum, as well [14]. Cross-sectional view of the design is given in Figure 1.4. Significance of this design is that it has a similarity with the proposed device of dissertation, high dynamic range. Although instead of a tuning fork, a plate resonator is utilized by Kinnell, dynamic range suggested is interestingly similar. Fusion bonding is utilized for vacuum packaging and quality factor of 35000 is observed for some of the samples. Sensitivity and scale is reported as, 30 Hz/kPa and 0-2 bar. And it is commented that generic fabrication process flow allows devices to have a high dynamic range.

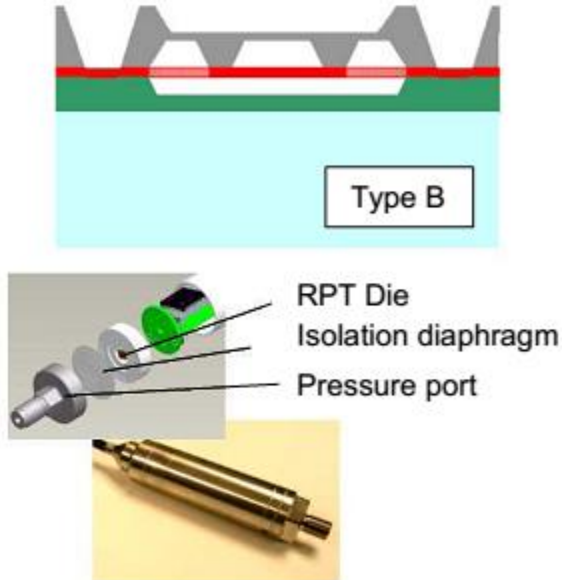

Figure 1.4 - Cross section view of a design proposed to have a high dynamic range of operation in hydraulic oil [14]

Although it is not stated clearly, it is likely that diaphragm thickness is modified through fabrication. Dissertation also states changing diaphragm thickness for this purpose.

To this point all of the described designs made use of a resonator which is parallel to diaphragm structure. Main advantage of such systems is fabrication simplicity. Because along with resonator, diaphragm can easily be fabricated within cleanroom, moreover silicon can be chosen as a diaphragm material and its superior mechanical properties improve design. But it comes with a price of low range because it is not possible to load the DETF structure until the point of buckling in parallel configuration.

There is only one design in the literature at the moment which claims to use a DETF structure in orthogonal position with the diaphragm. This is the most prominent device up to present which was nominated to be a breakthrough [6] and have a very high resolution (10 ppb). There are 3 main differences between this and proposed designs. Firstly, type of stress they are working with and secondly, material used. Proposed design works with silicon under compression, for which the sensitivity is greater, but former design uses quartz under tension. As a third difference, Bourdon tube depicted in Figure 1.5 is utilized in this design instead of a diaphragm.

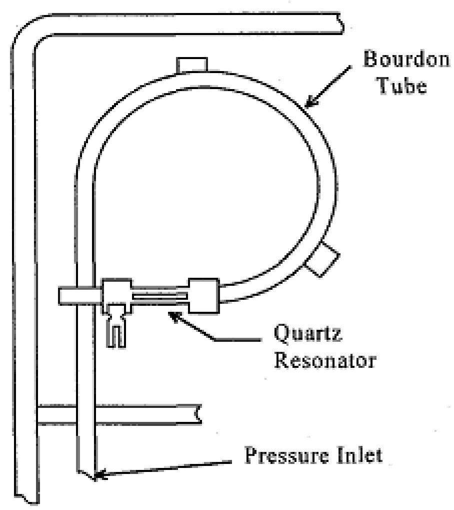

Figure 1.5 - State-of-the-art MEMS resonator pressure sensor obtained by using Bourdon tube instead of diaphragm [24]

1.4.2. Double-Ended Tuning Fork Sensor Applications

DETF has superior sensor properties compared to other types of resonators. When it is accounted that they have properties such as low hysteresis and long term stability, it is easy to understand why they are commonly adopted by many researchers. Moreover DETFs made out of quartz are readily available in the market which also suitable for some and decreases the burden of fabrication. Nonetheless, the most important two properties of DETF are associated with range and dissipative behavior. Firstly, tip of DETF can be deflected until the point of buckling which increases the range of device immediately. Secondly, as opposed to single beam resonators, tuning forks offer unique symmetrical property. Two tines of resonator are very weakly coupled via anchor. In turn, while tines are moving in opposing directions at anti-phase mode, anchor loss does not occur substantially which yields high quality factor. Consequently, DETF has gained many different application areas among sensors. As mentioned before, they are highly sensitive to presence of axial stress. But their sensitivity also depends on factors such as surrounding volume properties, mass changes, uneven vibration energy localizations and operation temperature [25, 26]. In this section application examples of DETF structure will be depicted with illustrations for comprehension and principles of operations will be described.

Aforementioned axial stress sensitivity has been utilized by several type of sensor. Among these are accelerometers, gyroscopes, magnetometer and such. But interestingly, many researchers made use of different principles in their studies. First example of this is that dependency of natural frequency on mass of resonator has been used by humidity sensors. An example is suggested [25] and it is reported that the proposed sensor has high sensitivity, fast response and good stability. The principle is derived by coating tines of DETF with sol-gel so as to catch humidity in the medium. This technique is very straight forward and easy to adopt. Another humidity sensor is reported to work under vacuum [26] and it has an intriguing working principle. The proof mass electrode of this sensor is coated with silicon dioxide and part of this oxide is open to atmosphere. As humidity of ambient increases, resistance of silicon dioxide decreases which leads to faster charge decay from proof mass electrode. Eventually, electrostatic spring softening term changes and frequency shift is observed.

Another very interesting sensor which relies on silicon DETF structure is introduced [27]. This sensor makes use of difference in vibrational energy localizations in the DETF in order to measure electrical charge. Moreover it is demonstrated that rather than sensing frequency shift, by using this approach, several order of magnitude larger sensitivity value is obtained. Two different resonators are coupled very weakly to each other by means of a beam as shown in Figure 1.6.

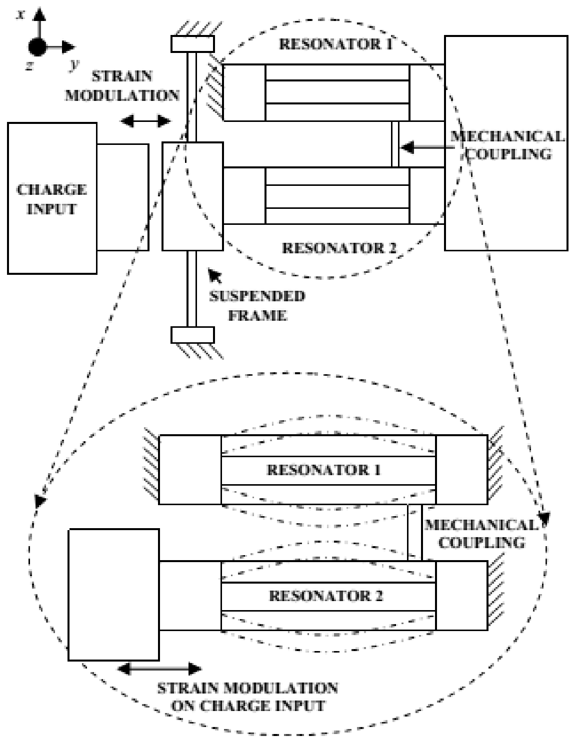

Figure 1.6 - Two resonators utilized for eigenvalue curve veering approach.

By this configuration when charge is applied, resonator 1 and 2 is affected indirectly and directly, respectively. Disturbance at one tine of resonator 1 causes energy confinement regions in DETF which alters its eigenstate. This phenomenon is named as curve veering and offers ultra-sensitive sensors.

Apart from presented applications researchers made use of axial stress sensitivity of DETF for building many different sensors including, temperature, strain, torque, tilt, magnetic field, gyroscope, accelerometer and force sensors [28-35]. Some of these sensors is demonstrated in the next portion of this section.

Temperature coefficient of modulus of elasticity is demonstrated to be around 60 ppm for single crystal silicon [36]. Hence as a matter of fact, natural frequency of a resonator is directly affected by temperature. Using this property of silicon high stability temperature sensor is reported [28]. It is a very straight forward application of DETF, though using 2 resonators side-by-side temperature resolution of 0.16 mK and relative frequency stability of 4.8 ppb is achieved.

Investigated torque and strain sensors are nearly identical [29, 30]. The resonators are both end fixed type and mounted on material of interest. Torque is sensed through shear strain while strain sensor's principle relies on measuring axial strain on the material.

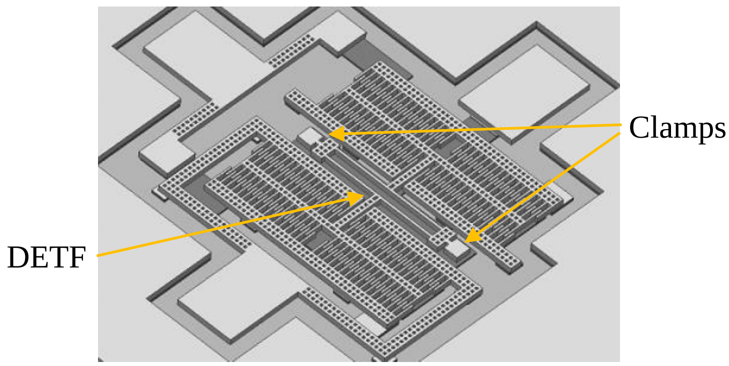

Figure 1.7 - Double clamped DETF strain sensor [30]

With addition of proof mass and to DETF structure accelerometers and tilt sensors can be obtained. Su *et al.* demonstrated and accelerometer design with 160 Hz/g by utilizing a proof mass between two DETF resonators [31]. Moreover Zou documented a tilt sensor with angular resolution of 500 nano-radian [32]. Both of the designs are pictured in Figure 1.8. It is seen that two designs are actually very similar in terms of alignment of levers, resonators and proof masses.

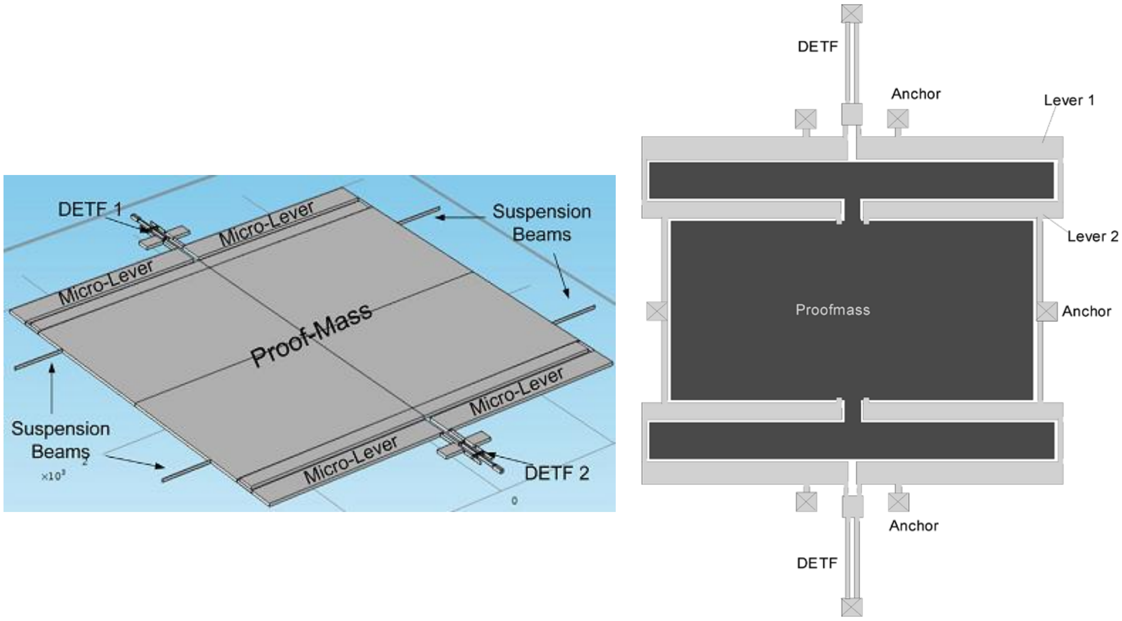

(a) (b)

Figure 1.8 - Examples of DETF structures with proof mass addition, (a) a tilt sensor and (b) an accelerometer [32] [31].

In tilt sensor of Zou, when the proof mass experience a gravitational field in the longitudinal axes of suspended beams shown in Figure 1.8, one of the resonators experiences a compressive stress while the other experiences tension. Similarly accelerometer's proof mass tries to move in the longitudinal directions of resonators upon application of acceleration. This motion of proof mass is conveyed to DETF resonators with a leverage mechanism, creating opposite types of stresses at them.

In another study rather than a proof mass, ends of a DETF resonator is fixed onto bars which are subjected to Lorentz force [33]. These crossbars and DETF alignment is shown in Figure 1.9(a). When a magnetic field in out-of-plane direction is experienced by bars, natural frequency of DETF shifts due to presence of axial stress. This study reports ultra-high quality factor (100,000) and a sensitivity of 215.74 ppm/T. Moreover it is predicted that this sensitivity can be as high as ten times, if geometry of device is chosen more carefully.

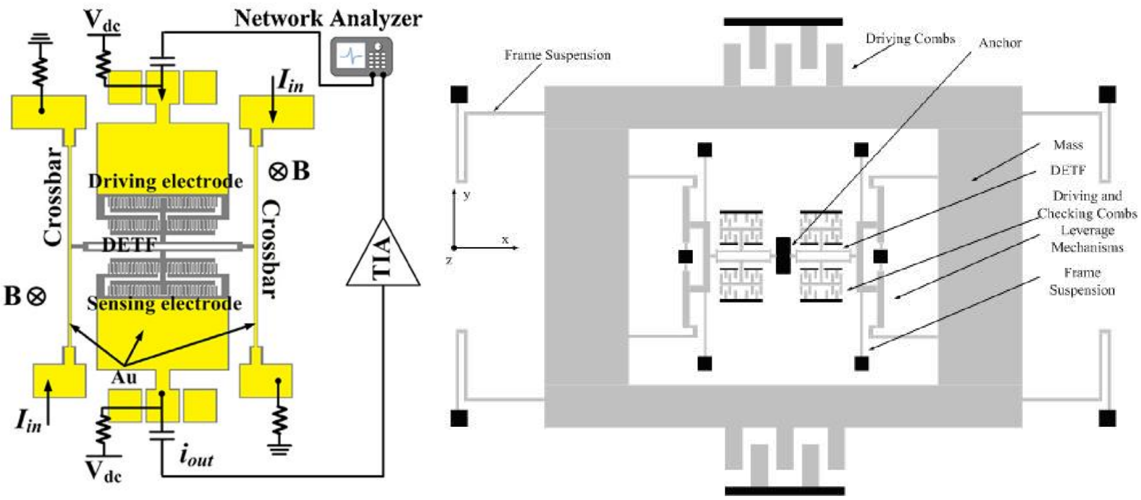

(a) (b)

Figure 1.9 - (a) Crossbar and magnetic field configuration of a DETF for measurement of magnetic field [33], (b) two DETF resonators used with levers and an encircling proof mass for measuring rotation

As a last example to its kind, DETF structure which is used as a gyroscope is presented [35]. This structure uses levers in order to amplify the motion of the proof mass. Proof mass is subjected to Coriolis force when a rotation is on out-of-plane axis. Finally levers convey amplified motion to longitudinal axes of 2 DETF resonators of which natural frequency is modified.

CHAPTER 2

RESONANT SENSING

Structures give large amplitude response at some certain frequency of excitation although the amplitude of excitation is low. This phenomenon is called as resonance and the frequency at which it occurs is named as natural frequency, ω_n.

In the absence of damping, natural frequency of a system can be defined as;

$$\omega_n = \sqrt{\frac{K_{eq}}{M_{eq}}} \tag{2.1}$$

According to (2.1) natural frequency of a system depends on mass and stiffness of it which gives the essential idea of resonant sensing. Although equation (2.1) is valid for various type of structures, in this study mechanical response of a DETF structure which is composed of two slender beams will be investigated in particular. If mass or stiffness of the beams is subjected to a change, natural frequency of the system also changes accordingly. Design principle of this pressure sensor relies on the latter, change in the stiffness. When an axial compressive load is applied to the ends of beams, especially tines in this case, transverse stiffness of the structure changes, decreasing the natural frequency of the resonator.

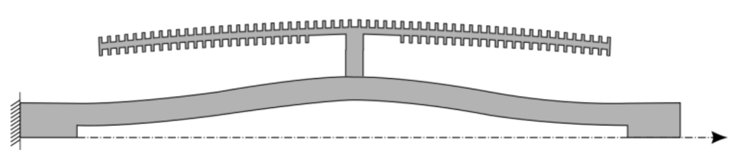

Figure 2.1 - Desired operational mode shape of DETF

Desired mode shape of DETF is shown in Figure 2.1 on half of the structure. The other half is symmetric about the longitudinal axis.

2.1. Theory of Resonant Force Sensing

As mentioned before, upon application of axial compressive force, stiffness of a tine changes. In this study, tine is a beam which is driven to its resonance with a transverse electrostatic force. Also 2 tines of DETF are assumed to have a symmetric shape about longitudinal axis at resonance, thus study of one tine only will be conducted.

Governing equation for response of such beam is given as;

$$\frac{\partial^2}{\partial x^2}\left(EI\,\frac{\partial^2 w(\mathrm{x},\mathrm{t})}{\partial x^2}\right)+\frac{\partial}{\partial x}\left(\frac{F_{app}}{2}\frac{\partial w(\mathrm{x},\mathrm{t})}{\partial x}\right)+\rho A\frac{\partial^2 w(\mathrm{x},\mathrm{t})}{\partial t^2}=P_e(\mathrm{x},\mathrm{t}) \qquad (\ 2.2\ )$$

where *EI* is the flexural rigidity, w is the deflection which is a function of axial position *x* and time *t*, F_{app} is the applied compressive axial force, ρ is the material density, *A* is cross sectional area of beam. Remaining $P_e(x,t)$ term is the harmonic driving force acting on the center of the beam transversally.

First term of this equation represents bending stiffness of the beam while the second term introduces tensional or compression stiffness. Lastly, the third term stands for inertial forces where ρA is the mass per length of tine.

At resonance, deflection *w* is associated with a mode shape and a modal coordinate term which are functions of *x* and *t*, respectively. Hence deflection can be written as;

$$w(\mathrm{x},\mathrm{t})=\phi(\mathrm{x})q(\mathrm{t}) \qquad (\ 2.3\ )$$

In above equation ϕ and q represents the mode shape and modal coordinate, respectively. For convenience $\varepsilon = x/L$ is defined and solution of the form is sought,

$$M_{eff}\ddot{q}+K_{eff}q=P_e(t) \qquad (\ 2.4\ )$$

When (2.3) substituted into (2.2) effective mass and stiffness terms can be found as;

$$K_{eff} = 2\frac{EI}{L^3}\int_0^{\frac{L}{2}}\left(\frac{\partial^2\phi}{\partial\varepsilon^2}\right)^2 d\varepsilon + 2\frac{F_{app}}{2L}\int_0^{\frac{L}{2}}\left(\frac{\partial\phi}{\partial\varepsilon}\right)^2 d\varepsilon$$

$$M_{eff} = 2\rho AL\int_0^{\frac{L}{2}}\phi^2 d\varepsilon + \sum_j m_j\left[\phi(\varepsilon_j)\right]^2 \tag{2.5}$$

where m_j and ε_j are masses and positions of capacitive plates at desired mode shape of tine. Mode shape function of a tine can be assumed as;

$$\phi = 16\varepsilon^3 - 12\varepsilon^2 + 1 \tag{2.6}$$

This function is driven geometrically from the shape of half of a tine at resonance itself which is shown in Figure 2.2.

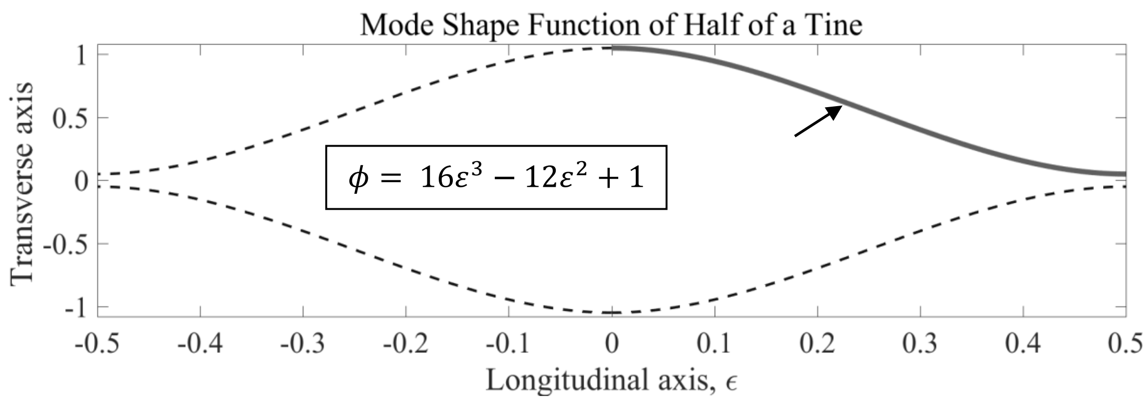

Figure 2.2 – Illustration of tines at desired resonance and corresponding mode shape function for half of a single tine

Half of the DETF is taken as a lumped mass and modal mass and stiffness can be found using (2.5) as follows;

$$M_{eff} = \rho h\left(\frac{13}{35}w_t L_t + w_{comb}L_{comb}n_{comb} + w_p L_p + w_c L_c\right)$$

$$K_{eff} = \frac{192EI}{L_t^3} + \frac{2.4F_{applied}}{L_t} \tag{2.7}$$

where n_{comb} is the number of comb fingers;

$$n_{comb} = 1 + \frac{L_p - L_{comb}}{2(L_{comb} + g)} \tag{2.8}$$

After calculating such parameters eigenvalue problem is obtained. But solution procedure to this problem will be presented in Ch. 3. On the other hand, result of an example problem will be given in this section in order to illustrate the frequency shift along with application of axial deflection. A simple beam having a length, width and height of respectively 867 µm, 16 µm and 35 µm is taken into account for this example. These dimensions actually belong to single tine of the fabricated DETF in this study. Natural frequency of beam with given dimensions can be found with accuracy by using a single degree of freedom model. And hence, when integrals in (2.5) are simplified and calculated for such beam and substituted into (2.1) natural frequency can be found. In Figure 2.3 result of axial deflection on natural frequency is exampled. Note that, negative axial deflection represents compressive force which decreases effective stiffness of the beam and therefore decreases the natural frequency.

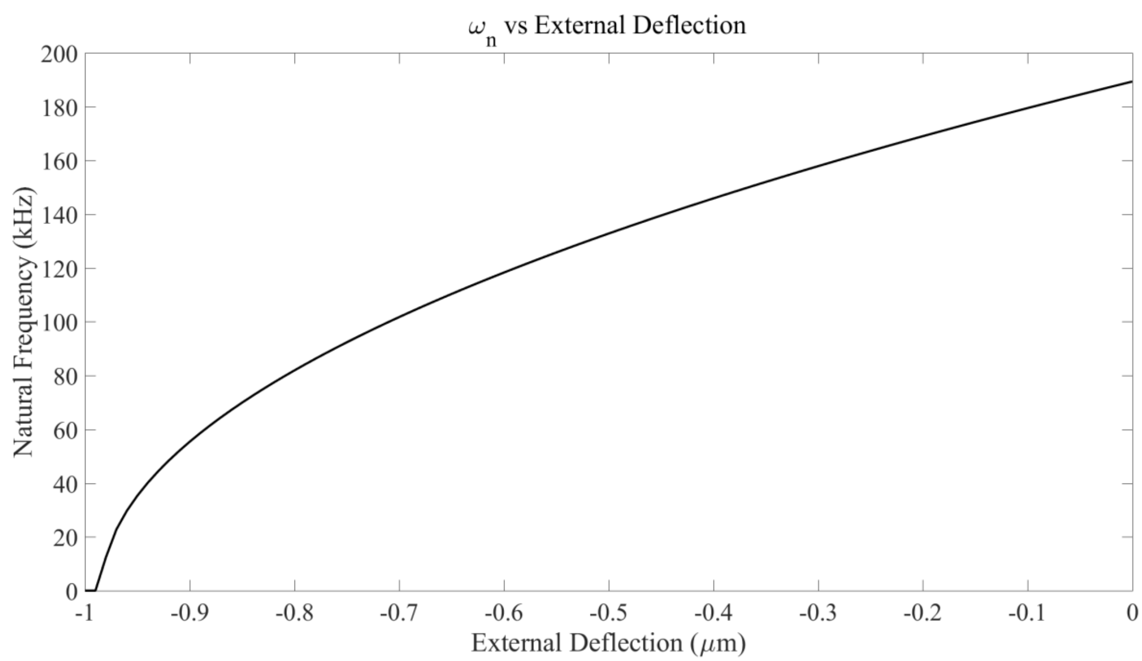

Figure 2.3 - Illustration of relation between axial load and natural frequency of a beam using single degree of freedom model

Frequency reaching zero at near -1 µm deflection states the point of buckling of the beam. Around this point, sensitivity i.e. slope of the natural frequency curve, is at its highest values, yet the voltage output acquired from capacitive plates are not sufficient for proper reading at this frequency range.

In order to show the response of the tines while applying an axial force at the end simple single degree of freedom system can be analyzed. Resulting frequency responses illustrate expected response of the sensor in hydraulic pressure tests. Equation of motion for a single degree of freedom system shown in (2.4) is;

$$m\ddot{x}_{(t)} + c\dot{x}_{(t)} + kx_{(t)} = F_{(t)} \tag{2.9}$$

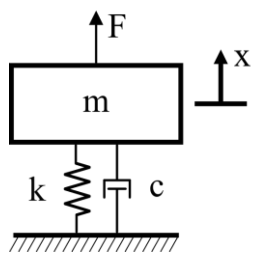

Figure 2.4 - Mechanical model of a single degree of freedom system

Assuming a harmonic forcing and response,

$$\begin{aligned} x_{(t)} &= Xe^{i\omega t} \\ f_{(t)} &= Fe^{i\omega t} \end{aligned} \tag{2.10}$$

Equation of motion becomes,

$$(-m\omega^2 + ic\omega + k)Xe^{i\omega t} = Fe^{i\omega t} \tag{2.11}$$

Then ratio of response to the forcing can be found as,

$$\frac{X}{F} = \frac{1}{(-m\omega^2 + \mathrm{k}) + i(c\omega)} \tag{2.12}$$

Which is complex function and has a magnitude of,

$$\left|\frac{X}{F}\right| = \sqrt{\frac{1}{(-m\omega^2 + k)^2 + (c\omega)^2}} \qquad (2.13)$$

Finally by dividing both parts of right hand side of the equation by k, response can be written as,

$$X = \frac{F/k}{\sqrt{\left(1-\left(\frac{\omega}{\omega_n}\right)^2\right)^2 + \left(2\zeta\frac{\omega}{\omega_n}\right)^2}} \qquad (2.14)$$

Under deflection stiffness and hence natural frequency terms changes, which affects the response as shown in,

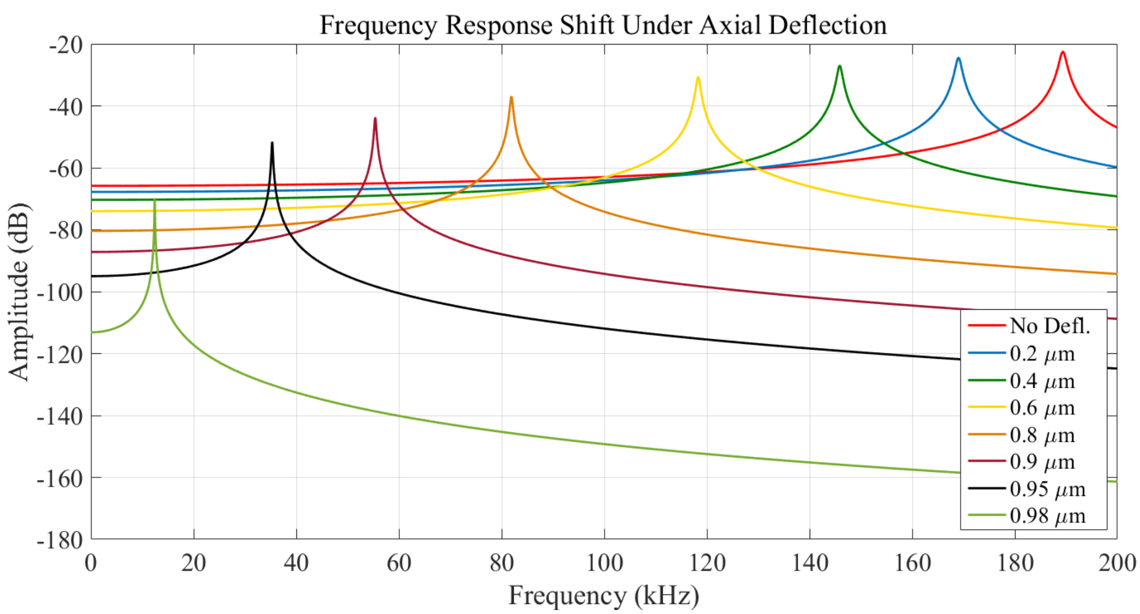

2.2. *Energy Loss Mechanisms*

For a system, if it is desired to avoid large response at its natural frequencies, system is damped accordingly. Dampers absorb undesired large kinetic energy of the system and converts it into other forms of energy. A well-known example to this can be the suspensions of vehicles which turns excess vibrational mechanical energy to heat energy through friction because the less vibration the more comfortable drive which is desired for vehicles.

However resonators are meant to vibrate largely. Hence for mechanical resonators decreasing amount of energy dissipated through dampers promotes better sensitivity and higher signal-to-noise ratio. Moreover the required power input to the system decreases due to less energy dissipation. This dissipation is directly related with damping ratio of the system, c. However, commonly used definition while dissipative behavior of a system is being described is named as quality factor, Q, is inversely related to c as;

$$Q = \frac{\omega_n M_{eq}}{c} \qquad (2.15)$$

As (2.15) suggests higher quality factor means a less dissipative resonator with superior mechanical and electrical properties. In this study the pressure sensor of interest is designed to operate in air. Since air between gaps of the structure acts as damper to the system, it is related with the energy loss. Actually, when a resonator operates in atmospheric pressure, losses due to presence of air generally dominates other intrinsic losses such as thermoelastic damping (TED), support loss, surface loss etc. Therefore in this design Q due to air damping will be the largest portion that defines total Q. In this section quality factor estimations used in optimization computations are described.

Damping due to air is an extrinsic damping and can be manipulated by design. Depending on choice of parallel plate or lateral comb finger actuation and detection, damping characteristics changes. If the design makes use of change in the distance between electrodes for detecting electric field change, squeeze film damping occurs due to elasticity of air. However, if detection of electric field results from change of overlapping length of the electrodes, then rather than squeezing, air rolls between plates. The energy dissipation is due to viscous forces in these laterally moving plates. The latter is named as sliding air damping, and in this section effect of these two types of air damping will be compared since it is important to decide on the working principle of capacitive sensing and detection.

2.2.1. Sliding Air Damping

Two types of sliding air flow should be taken into account when modeling the flow between two laterally driven plates. Specifically, these are named as Couette-type flow and Stokes-type flow. According to Wang for very small gaps of low frequency applications Couette-type flow is appropriate while Stokes-type flow is applicable to high frequency regime [37]. Although application of this study covers both, Couette-type flow is much more straightforward for analysis, moreover it is reported that Couette-type flow assumption works with accuracy for 2 µm gap comb fingers [38]. Therefore Couette-type flow is chosen for modeling. This flow type assumes a laminar flow between comb fingers. In Figure 2.5 top and side view of a lateral comb finger is given and resistances related to fluid flow are presented.

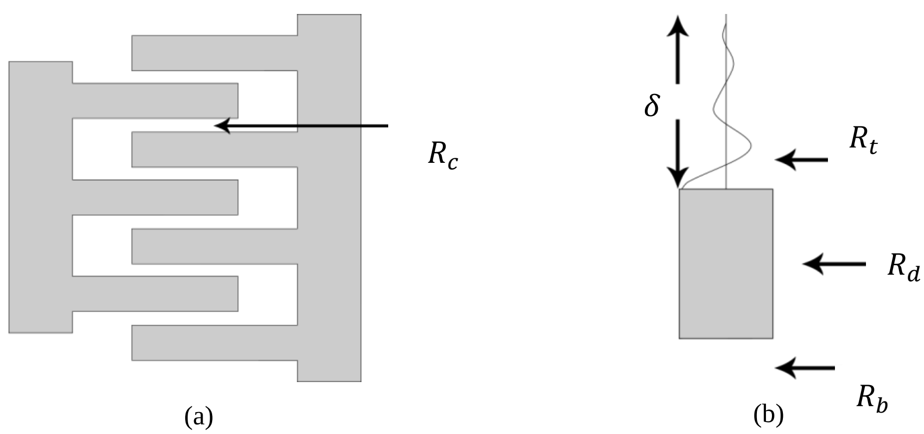

Figure 2.5 - (a) Top and (b) side view of comb fingers with the air resistances shown

R_c, states the resistance due to sliding flow between comb fingers and is related with quality factor Q_c whereas, R_t, R_d and R_b are the top, direct and bottom resistances and related with corresponding quality factors. In Figure 2.5, δ represents the penetration depth, which is defined as beyond this distance fluid can be assumed as stationary. It is related with the oscillation frequency of the plate and kinematic viscosity of the fluid as [38];

$$\delta = \sqrt{\frac{2\nu}{\omega}} \tag{2.16}$$

where ν is kinematic viscosity of the fluid. For air at room temperature and the plates oscillating with a frequency greater than 90 kHz, δ is less than 10 µm. Since the capacitive plates are released and have more than 10 µm fluid on top and below, δ is taken in to consideration while calculating Q_t and Q_b. These two quality factors are actually assumed to be equal because of the same penetration depth. They are calculated as [38];

$$Q_t = Q_b = \frac{\delta\sqrt{M_{eff}K_{eff}}}{\mu A_s} \tag{2.17}$$

where, μ is viscosity of air which is assumed to be equal to $17.9 \times 10^{-6}\ Pa \cdot s$ and A_s stands for the damping related surface of the resonator. In this context, this is total surface area of vibrating portion including, tines and capacitive plates. Since the flow between comb fingers are also assumed to be Couette-type flow, Q_c is calculated in the same manner;

$$Q_c = \frac{g\sqrt{M_{eff}K_{eff}}}{\mu A_c} \tag{2.18}$$

This time g is the gap between fingers which is 2 µm, and A_c is the total overlapping area of comb fingers. Q_d, however cannot be calculated and left for estimation after the tests. Finally, total quality factor with the assumption of sliding air damping can be calculated in compliance form;

$$\frac{1}{Q_{total}} = \frac{1}{Q_c} + \frac{1}{Q_t} + \frac{1}{Q_b} \tag{2.19}$$

2.2.2. Squeeze Film Damping

Capacitive plates may be utilized instead of comb fingers. If such decision is made, then squeeze film damping will be present between the parallel plates of capacitances. While estimating quality factor due to squeeze film damping, it should be noted that there exists a secondary effect, the elasticity of air alters the natural frequency of the structure. Therefore along with damping coefficient of air, stiffness also should be of concern and added to effective stiffness before estimating corresponding quality factor. As mentioned before squeeze film damping occurs due to elasticity of air between the plates. This air is exposed to constantly oscillating pressure difference due to harmonic motion which causes energy dissipation.

Along with that, viscous energy dissipation also takes place since the slip at the other boundaries of the resonator still remains. Thus, Q_t and Q_b which are found by (2.17) still valid for parallel plate decision, too.

In order to find the quality factor damping coefficient and spring constant of air should be calculated first. And procedure of this calculation is given neatly in [39] and it starts with calculation of squeeze number, σ.

$$\sigma = \frac{12\mu h^2 \omega_n}{Pg^2} \tag{2.20}$$

Where P is atmospheric pressure which is equal to $1.01 \times 10^5\ Pa$. Accordingly stiffness and damping coefficient is obtained by;

$$\begin{aligned} K_{air} &= 2\frac{64\sigma^2 P L_p h}{g\pi^8}\frac{1}{\left[1+\left(h/L_p\right)^2\right]^2+\sigma^2/\pi^4} \\ c_{air} &= 2\frac{64\sigma P L_p h}{g\pi^6\omega_n}\frac{1+\left(h/L_p\right)^2}{\left[1+\left(h/L_p\right)^2\right]^2+\sigma^2/\pi^4} \end{aligned} \tag{2.21}$$

After calculating stiffness term, K_{air}, natural frequency should be calculated again by appending this value to obtain new effective transverse stiffness of structure. Then when damping coefficient is calculated, quality factor for parallel plates, Q_p can immediately be found by (2.15). Finally total quality factor when parallel plates are used can be found by substituting Q_C with Q_p in (2.19).

2.3. *Summary*

In this chapter some of the equations and concepts related with resonant sharing is shared. In order to handle the concept similar to optimization routine, mode shape is assumed and effective mass and stiffness values are derived. Using these expressions, decrease of natural frequency of a simple beam with applied compressive loading is presented. Additionally, single degree of freedom model is adopted and change of frequency response of the same beam with applied compressive loading is estimated. Moreover air damping is investigated in two parts, sliding air damping and squeeze film damping. Relations for estimating quality factors and damping coefficients are revealed. In conclusion, relevant background knowledge for calculations in chapter 3 are provided in this chapter.

CHAPTER 3

DESIGN OPTIMIZATION

In this chapter design objectives and considerations are given in detail. Design and stress analysis of pressure port and modal and buckling analysis of resonant structure is explained.

The design of this pressure sensor can be divided into 2 sub-functions,

- Design of a DETF structure capable of overcoming large deflections such as 100 μm without buckling,
- Design of a package capable of deflecting DETF when an external hydraulic pressure is applied in desired range of deflection,

3.1. Design of the Package

A very simple yet effective package is necessary otherwise manufacturing of the package and implementation of the structure on to the package would be too difficult. Therefore package design kept very lean. Package is consisting of basically 3 elements. These are, a hollow cylinder to slide sensing element in, a pressure port module which transfers exterior pressure to the sensing element and a gasket for sealing the hydraulic fluid. Exploded and assembled CAD views of the package are shown side-by-side in Figure 3.1.

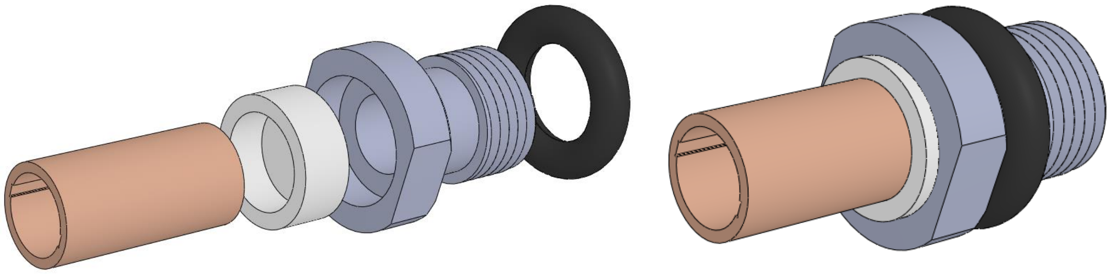
(a) (b)

Figure 3.1 - (a) Exploded and (b) assembly view of pressure port

Main design objective of package is that, it has to endure at least 100 Bars of hydraulic pressure while at the same time deflection of the diaphragm in the pressure port should be as large as possible. But there are two constraints for the design; first, maximum stress experienced by diaphragm of pressure port has to be smaller than 138 MPa. This value is chosen for an aluminum 6061 diaphragm with yield strength of 276 MPa in order to obtain a safety factor of 2. Thus, stress and deflection analysis is conducted both analytically and numerically for diaphragm. Secondly, diameter of the diaphragm should not exceed 6.2 mm and this value depends on the maximum diameter of the corresponding port of testing equipment. Lastly, threads of the pressure port which engages into hydraulic circuit have to endure 100 bars.

Diaphragm can be assumed as a circular plate with clamped edges. According to Kirchhoff-Love plate theory, maximum stress occurs at the boundary of the plate. Magnitude of stress at clamped edge can be found from [40],

$$\sigma_{\max} = \frac{3}{4}\frac{\mathrm{Pr}^2}{h^2} \tag{3.1}$$

where P is the magnitude of uniform pressure in N/m^2, r is the radius of the plate and h is thickness of the diaphragm. Maximum deflection under uniform loading for this type of loading occurs at the center point and equal to [40],

$$\omega_{\max} = \frac{\mathrm{Pr}^4}{64D} \tag{3.2}$$

D is flexural rigidity in this equation and can be calculated using following,

$$D = \frac{Eh^3}{12(1-\nu^2)} \tag{3.3}$$

with ν being Poisson Ratio. When equations (3.2) and (3.3) are combined and material properties of structural steel are inserted, required thickness of the diaphragm can be found.

It is necessary to find the diaphragm with the smallest thickness, with 6.2 mm in diameter which can endure 100 bars. Under these conditions maximum achievable deflection satisfying σ_{max} = 138 MPa is obtained as center deflection of 6.06 µm with a diaphragm thickness of 0.72 mm. 138 MPa of compressive stress occurs in under maximum pressure conditions which is satisfying the maximum stress criteria for the design.

Another weak point of the pressure port is the threaded portion of the fastener part. Safety factor for the threads under these conditions can be calculated with the procedure given below. In order to calculate the force acting on threads, first thread area is calculated as such,

$$A_{th} = 0.5\pi L_e (D - 0.64952\ p) \tag{a}$$

where is engagement length, D is major diameter and p is size of pitch in millimeters. L_e, D and p are 4.5, 9.72 and 0.907 mm, respectively, for the fastener that fits into testing equipment. Then stiffness of bolt element and other members of the connection have to be found. Stiffness of bolt can simply be calculated as,

$$k_b = \frac{A_{th} E}{L_e} \tag{b}$$

Also in order to find joint stiffness, stiffness of other members, k_m, should be found. Since, k_g, stiffness of gasket is much less than stiffness of other elements of joint, stiffness of members is assumed to be,

$$k_m = k_g \tag{c}$$

where k_g is assumed to be around 260 N/mm. And hence stiffness term of the joint, C, is calculated,

$$C = \frac{k_b}{k_b + k_m} \quad \text{(d)}$$

Force on the joint exerted by hydraulic pressure is,

$$F_{fluid} = \pi r^2 P_{ext} \quad \text{(e)}$$

Finally resulting bolt force is,

$$F_{rb} = CF_{fluid} + F_{preload} \quad \text{(f)}$$

With the assumption of initial load, $F_{preload}$, equals to 5 kN, safety factor is calculated as,

$$n = \frac{\sigma_y A_{th}}{F_{rb}} \quad \text{(g)}$$

In order to achieve higher safety factor for threaded portion, this part of the pressure port is manufactured from steel. In other words, pressure port is decided to consist of two different parts with interference fit, aluminum for diaphragm to achieve higher deflection without yielding and steel for threaded portion to achieve better safety factor.

Steel part of the pressure port is readily available in the market and with few machining steps it is prepared for use. Specifically type of that material is free cutting steel 9S 20. When material properties of 9S 20 are inserted in equations above safety factor is found to be 2.89.

3.2. Design of Resonant Structures

This design consists of a DETF element which is microfabricated and a package which contains the DETF element and its connections with the outer domain. The package is manufactured with conventional manufacturing methods with very large precision while DETF is fabricated with microfabrication methods at a sub-µm precision.

Thus, DETF element is designed to have mechanical springs to bear axial deflection of 100 μm at least without buckling. Main motivation of this is to protect the sensing element. By itself, DETF is very vulnerable to buckling while getting in contact with diaphragm, but with a set of spring elements which can absorb large portion of this deflection, structural integrity of DETF is secured. This also helps to reduce the effect of misalignment while mounting DETF inside package. Aforementioned spring elements are in the form of folded beam and present at only one end of DETF. Illustrative drawing of the designed spring & DETF structure is shown in Figure 3.2.

It is also important to eliminate transverse loads which are dangerous for DETF because they can easily damage tip of sensing element. If misaligned, DETF tip may miss where it is supposed to touch on the package and experience transverse load. Thus, springs are also used in supporting a roller which prevents most of the transverse deflection from reaching to the tip of the sensing element

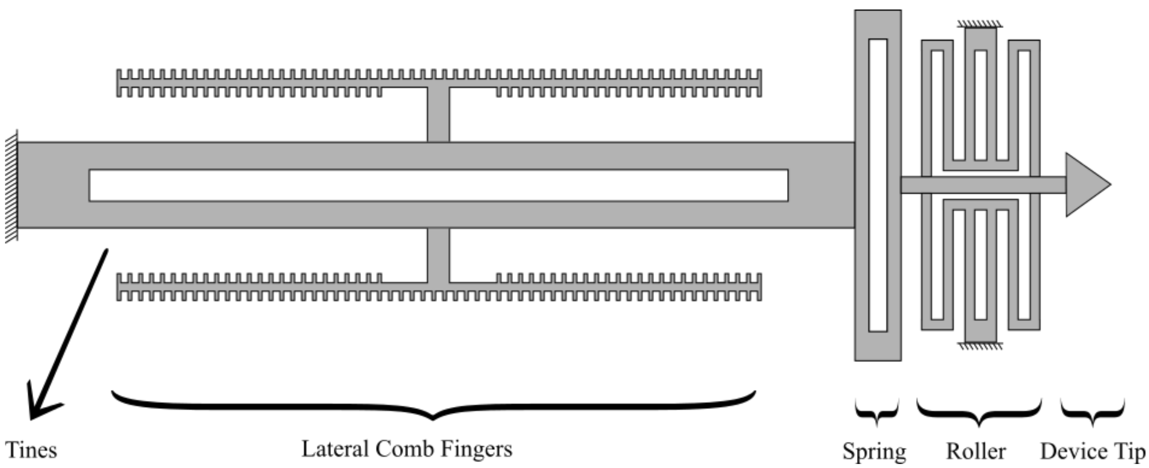

Figure 3.2 - Illustration of DETF with lateral comb fingers and its complementary springs and rollers

Another point in the design is to use lateral comb fingers for capacitive detection since squeeze film damping is inevitable for parallel plate detection under atmospheric operation conditions. Two types of capacitances for capacitive plates are shown in Figure 3.3. Comb finger type causes air damping due to sliding fluids between the combs. Sliding air damping is more desired than squeeze film damping because of the relatively lower energy dissipation under atmospheric pressure. Thus, overall quality factor is expected to be greater for lateral comb fingers.

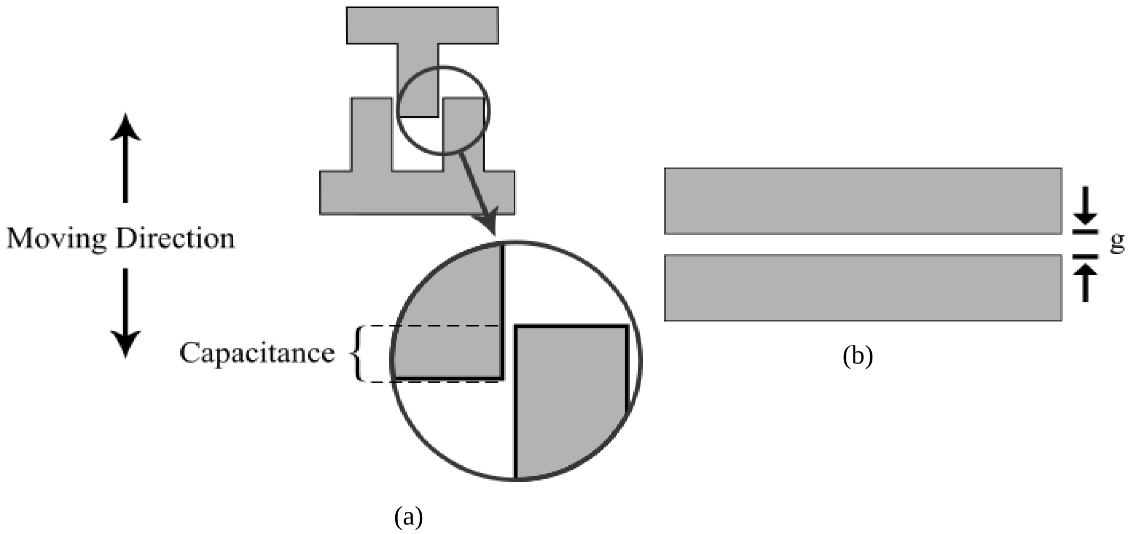

Figure 3.3 - Illustrations of (a) lateral comb finger and (b) parallel plate configurations

Dimensions of devices are defined by an optimization algorithm of which objective is to achieve the best sensing resolution. In order to obtain variety of devices, different limitations are set, hence devices with different dimensions are resulted for each.

Furthermore, design includes simulations for verifying the model on which optimization code is based. Moreover effect of axial load application on the tip of device is simulated in order to provide design criteria that enables 100 µm tip deflection. Therefore all of the devices are verified to bear a compressive deflection of 100 µm without buckling.

In detail, Solid Mechanics module of COMSOL Multiphysics 5.0 package is used for simulation purposes. This module allows to run eigenfrequency analysis which uses the geometrical and material properties in order to find desired mode shapes and corresponding natural frequencies. But specifically, pre-stressed eigenfrequency analysis is used to obtain results of axial loading and natural frequencies of the devices. It is allowed to compute stationary loaded case and frequency analysis simultaneously with this study mode. Equations which are handled by this module and study mode are known as Navier-Cauchy equations which are commonly used to solve linear elasticity problems.

3.2.1. Design Constraints

Tines are the key elements of resonant structure and important specifications such as sensitivity, quality factor, minimum detectable pressure, natural frequency, output voltage are directly depends on the geometry of tines. Therefore optimization of tine geometry states high importance. In order to optimize the performance of device, a MATLAB code is generated. This code optimizes tine width and length. Code seeks the best possible values of these parameters between pre-set upper and lower bounds while satisfying certain limitations and maximizing some of the mechanical and electrical properties of sensing element.

Purpose of limits is to design a device that can be tested properly with the equipment in hand. There are 2 types of limitations for design, these are;

- Output voltage is greater than 25 mV,
- Natural frequencies of devices are no greater than 90 kHz,

Objective function of the optimization routine is to find the tine geometry which yields maximum value for product of sensitivity and quality factor. This function is set basically because of two reasons. First, atmospheric working conditions drastically decrease quality factor of the device. Secondly, spring element which aims to protect the device, decreases sensitivity by nearly 100 times as a drawback.

Desire for achieving high quality factor eliminates all devices with parallel plate configuration because with squeeze film damping, quality factor is calculated to be around only 10. Then due to imperative presence of lateral comb fingers, output voltage becomes a concern since overlapping type of capacitance does not change as much as varying gap does with lateral motion. This problem can be solved by having longer capacitive plate since this increases number of comb fingers. As a consequence, atmospheric operation environment implies a condition such that capacitive plates have to be sufficiently long. For this study capacitive plate length is set to 0.9 times the tine length for all geometries.

3.2.2. Geometrical Optimization Procedure

It is possible to model the system as a single lumped mass and include mass of capacitive plates in (2.5), but since the length of the capacitive plates are relatively large, 90% of a tine in length, assumption that they are rigid bodies actually imposes inaccuracy on the optimization. With this in mind, solution of (2.4) and (2.5) handles the system as a single degree of freedom one by lumping all mass elements at one point and omitting the behavior of capacitive plates. In order to show the effect of this inaccuracy, and discuss acceptability of this approach, comparison of single degree of freedom model with finite element analysis results is made under optimization results heading.

Theoretical background of calculations with procedure is given in the following pages with explanations. In these calculations modal analysis of half of the DETF is conducted and hence half of structure is modelled since the mode shape shown in Figure 3.4(a) which is sought is symmetric with respect to longitudinal axis.

Single DOF mechanical model used is given in Figure 3.4(b). m_1 stands for lumped mass of upper half of the structure and k_1 represents equivalent stiffness of a tine which is equal to stiffness of a both ends fixed beam at the middle point. Also damping coefficient is included in the model as c_1. This is the same model investigated in Ch. 2.

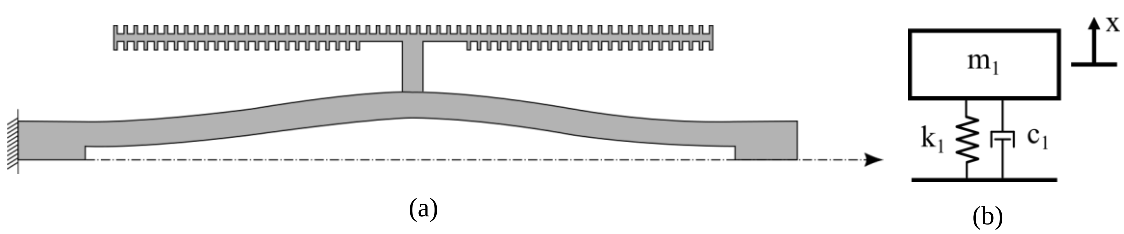

Figure 3.4 – (a) Modelled part of the DETF in desired mode shape (b)Single degree of freedom model which consists of lumped mass of tine, connection beam and comb branches

While dimensions of tines are kept as parameters to the optimization routine, for each possibility located between parameter bounds, modal analysis is conducted. This brings natural frequencies as well as corresponding mode shapes. Then sensitivity, output voltage, minimum detectable pressure is calculated. Moreover calculations for estimation of quality factor takes place in this code, too.

Before starting explanation of procedure, dimensions of the structure are given in Figure 3.5. These notations can be defined swiftly as L being length and w being width and subscripts, p, t, c, and comb belongs to plate, tine, connector and comb, respectively.

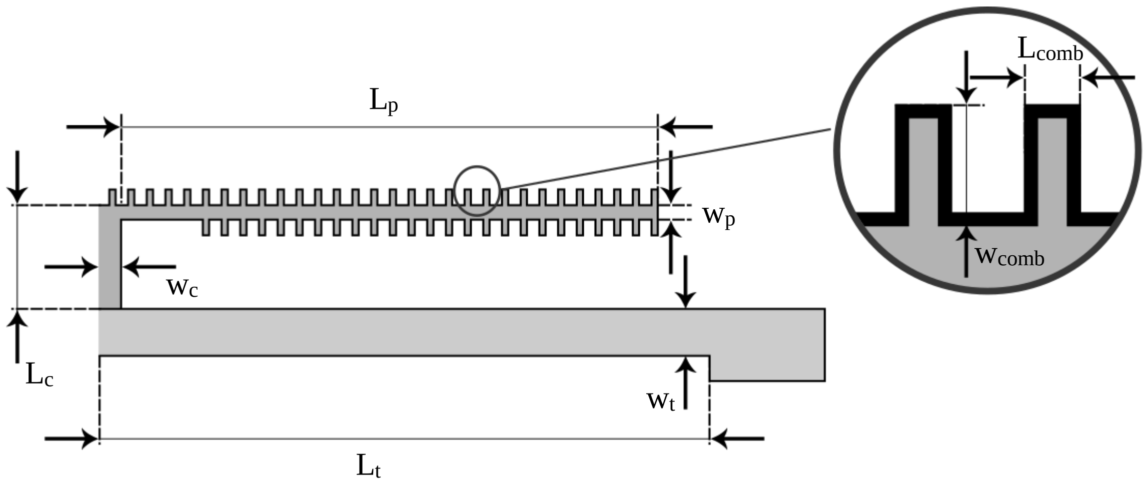

Figure 3.5 - Dimensions of the model

The calculation progress starts with computing m_1 & k_1 values for all possible geometries within specified range. This step is simply computed according to (2.7). After that by using (2.1) natural frequency of the structure is estimated. It should be noted that, in this mode, only tine is assumed to be a flexible body and moving in transverse direction harmonically.

After this step important specifications of design are calculated and estimated for all combinations of L_t and w_t. The computational procedure explained above runs for every geometrical possibility and finds natural frequency of the desired mode shape.

Sensitivity term is the rate of change of natural frequency with respect to applied pressure. Thus unit of this term is simply pressure unit per Hz. It can be calculated numerically as,

$$Sensitivity = \frac{\omega_{n,0} - \omega_{n,\delta}}{0 - P_\delta} \qquad (3.4)$$

where P_δ and $\omega_{n,\delta}$ stands for amount of pressure and natural frequency at that pressure. By setting P_δ to a small amount such as 10 nbar sensitivity can be estimated for single degree of model numerically. Tough in a single degree of freedom system it can be found by substituting (3.2) & (2.7) into (2.1) and taking derivative with respect to P as;

$$\frac{\partial \omega_n}{\partial P} = \frac{\partial \omega_n}{\partial x}\frac{\partial x}{\partial P} = \frac{1.2 K_{DETF,axial}}{M_{eff}\,\omega_n L_t}\frac{r^4}{64D} \qquad (\,3.5\,)$$

Output voltage is another important factor and states significance for quality of test results. Its calculation is relatively easier for lateral comb finger than parallel plate configuration because capacitance change linearly with respect to motion of tines. Therefore non-linear term related with parallel plate approach is absent for lateral comb finger configuration. In order to calculate V_{out}, current output due to alternating capacitance should be calculated first. Capacitance change between sense electrode and comb fingers of the resonator is found as;

$$C = 2\left(\varepsilon_0 \frac{(L_O + x)h}{g} 2n\right) - C_0 \qquad (\,a\,)$$

$$i = \frac{\partial q}{\partial t} = \frac{\partial}{\partial x}(CV) = \frac{\partial C}{\partial x}\frac{\partial x}{\partial t}V_{DC} + \cancelto{0}{\frac{\partial V}{\partial t}}C \qquad (\,b\,)$$

where,

$$\frac{\partial C}{\partial x} = \frac{4n\varepsilon_0 h}{g} \qquad (\,c\,)$$

$$x = A\sin(\omega t) \qquad (\,d\,)$$

$$\frac{\partial x}{\partial t} = A\omega\cos(\omega t) \qquad (\,e\,)$$

Figure 3.6 shows how resonator motion is converted into voltage. Trans-impedance amplifier circuit is connected to sensing electrode of resonator and current in (b) converted to voltage output. As a remark $\partial V/\partial t$ in (b) is zero because proof mass voltage is applied in DC form and thus does not change over time. Therefore (b) simplifies.

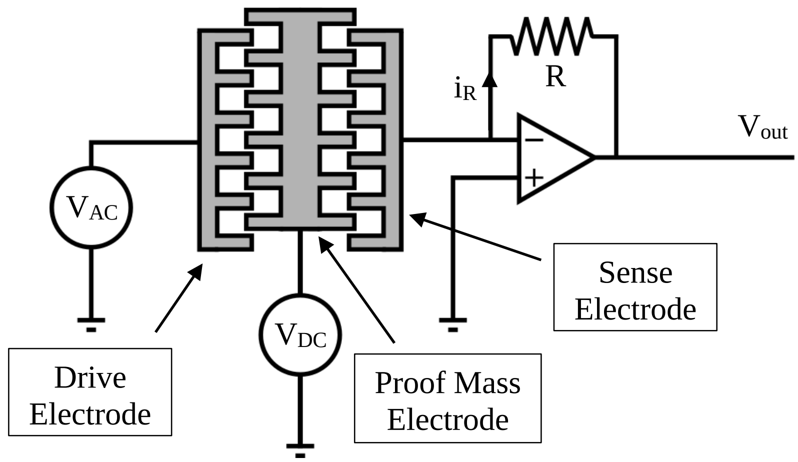

Figure 3.6 - Trans-impedance amplifier shown with resonator

Voltage output for trans-impedance amplifier configuration with $i = i_R$ is;

$$\boldsymbol{V = -i_R R} \tag{f}$$

Therefore V_{out} results as;

$$V_{out} = -R\frac{4n\varepsilon_0 h}{g}V_{DC}A\omega\cos(\omega t) \tag{3.6}$$

Minimum detectable pressure is another important specification for sensor. Moreover proposed sensor has superior resolution estimation when compared with the best in literature. Resolution depends on geometry of resonator and pressure port and noise for this sensor. In this section relation of minimum detectable pressure with resonator structure and amplifier noise is explained.

It is assumed that V_{out} is effected by noise, V_{noise}, in the worst possible way. For this scenario there should be a 90° phase between these two vectors as shown in Figure 3.7. This is the scenario in which V_{out} is deviated the most. V_{noise} is assumed to be a white noise due to thermal noise and amplifier noise. Then V_{noise} can be calculated as explained by Torrents *et al.* [39];

$$V_{noise} = \sqrt{4k_B TR_{amp} + e_n^2 + R_{amp}^2 i_n^2}\,\sqrt{\Delta f} \tag{3.7}$$

Utilized amplifier which is Texas Instrument's LF-353 has noise properties as follows;

$$Input\ Noise\ Current\ (i_n): 0.01\ pA/\sqrt{Hz}$$

$$Input\ Noise\ Voltage\ (e_n): 25\ nV/\sqrt{Hz}$$

In equation, T refers to temperature of environment in K and k_B is Boltzmann constant being equal to $1.381 \times 10^{-23}\ J \cdot K^{-1}$. $\sqrt{\Delta f}$ stands for the bandwidth of noise measurement and chosen as 100 Hz for this calculation.

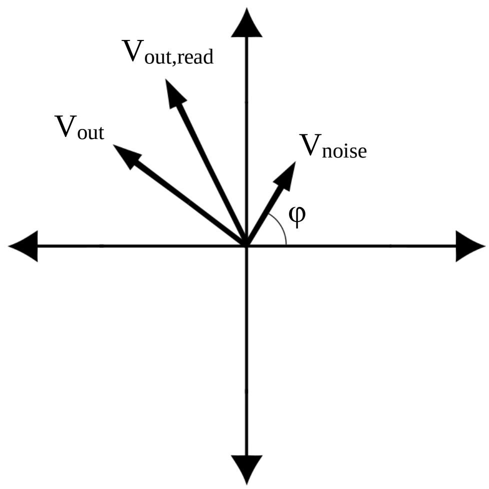

Figure 3.7 – Vectoral illustration of output voltage, voltage noise and read voltage at the worst case

Then read effective voltage output, $V_{out,read}$ can be written as;

$$V_{out,read} = \sqrt{V_{out}^2 + V_{noise}^2} \cos\left(\omega t + \phi + \frac{\pi}{2} + \arctan\left(\frac{V_{noise}}{V_{out}}\right)\right) \quad (3.8)$$

It is seen that, noise with phase φ, deviate V_{out} with a phase of $\Delta\varphi_{noise}$ which is,

$$\Delta\varphi_{noise} = \arctan\left(\frac{V_{noise}}{V_{out}}\right) \quad (3.9)$$

And this phase deviation also can be expressed as follows,

$$\Delta\varphi_{noise} = \frac{\partial\varphi}{\partial\omega}\Delta\omega_{noise} \quad (3.10)$$

At resonance, derivative of phase with respect to frequency is,

$$\left.\frac{\partial\varphi}{\partial\omega}\right|_{\omega=\omega_n}=\frac{2Q}{\omega_n} \qquad (3.11)$$

Therefore $\Delta\omega_{noise}$ equals to,

$$\Delta\omega_{noise}=\frac{\omega_n}{2Q}\Delta\varphi_{noise} \qquad (3.12)$$

Finally minimum detectable pressure can be found by dividing this frequency noise by sensitivity term, hence using (3.5), (3.9) and (3.12), Δ_{min} is found as;

$$P_{\min}=\frac{\Delta\omega_{noise}}{Sensitivity} \qquad (a)$$

$$P_{\min}=\frac{\arctan\left(\frac{V_{noise}}{V_{out}}\right)\frac{\omega_n}{2Q}}{\frac{1.2K_{DETF,axial}}{M_{eff}\,\omega_n L_t}\frac{r^4}{64D}} \qquad (3.13)$$

Moreover quality factor estimation takes place in optimization routine too. Calculation of quality factor is based on theory presented in Chapter 2. But both of the effects of air damping which are squeeze and sliding film damping is present on the design. Therefore both are taken into account during estimation.

Sliding air damping occurs between comb of capacitive plates and electrodes. Quality factor relating to this type is calculated in optimization routine by using (2.15). Also there arises squeeze film damping effect between the faces of electrodes and capacitive plates from where combs connect. Although this distance is relatively large (8 µm), since squeeze film damping is a powerful loss component, quality factor gets affected. In order to estimate quality factor due to squeeze film damping between these (2.20) and (2.21) is used and both of the quality factors are combined,

$$\frac{1}{Q_{overall}}=\frac{1}{Q_{squeeze}}+\frac{1}{Q_{sliding}} \qquad (3.14)$$

3.2.3. Optimization Results

As mentioned before optimization resulted in a design which has the maximum quality factor multiplied by sensitivity of the device. Therefore (3.5) and (5.1) are taken into account when defining the dimensions of the device. In Table 3.2 results of the optimization code is given. The results includes estimation of some of the other important electrical and mechanical properties.

Moreover in order to visualize how optimization code works, the some of the internal results are shown in below figures. For an interval chosen to define tine width and length, the code computes all the properties given in Table 3.1. Then filters out results which cannot satisfy the desired voltage output and natural frequency values. Finally, it picks the best possible design dimension to achieve maximum of the objective function of which surface plot is shown in Figure 3.12.

Optimization routine is forced to choose for tine length and width between 500-1200 µm and 10-20 µm, respectively. Resistance of trans-impedance amplifier is chosen as 1 MΩ and proof mass voltage is set to 15 V DC. Geometrical specifications are also given in

Table 3.1 - Constants fed to the optimization routine

Connector Plate Width	w_c	20 µm
Connector Plate Length	L_c	120 µm
Capacitive Plate Width	w_p	w_t
Capacitive Plate Length	L_p	$0.9 \times L_t$
Comb Width	w_{comb}	11 µm
Comb Length	L_{comb}	5 µm
Comb Gap	g	2 µm
Comb Overlap Length	L_{ov}	3 µm

And corresponding results are presented in Table 3.2;

Table 3.2 - Resulting design properties of optimization routine and its estimated electrical and mechanical properties.

Properties	Design
Natural Frequency (kHz)	89.99
Tine Width (µm)	16.50
Tine Length (µm)	866.70
Capacitive Plate Length (µm)	780.00
Number of Drive Combs	55
Output Voltage (mV)	25.05
Quality Factor	340

Intermediate results are illustrated in following figures in order to explain how limits work and optimization routine choose best possible design geometry between boundary limits.

The following figures can be confusing because of the stepped edge of the surface plots. However notice that these stepped edges are only present at the tine length axis of the graphs. Main reason of that is that design constraint about capacitive plate length. Remembering that capacitive plate length is set to 90 % of tine length, these stepped edges can be related to number of comb fingers. Since comb fingers have certain separation in between when capacitive plate length changes as much as this separation one comb finger is added to or removed from design. More specifically, this separation is set as 11 µm and at every 11 µm of change in length number of comb fingers change by 1. This causes a steep change in effective mass results in stepped edges on the length axes of plots.

Surface plots of two different limiting factors, voltage output and natural frequency is shown in Figure 3.8 and Figure 3.9. It can be deduced from these two figures that, designs are restricted to have natural frequency below 90 kHz and voltage output greater than 25 mV.

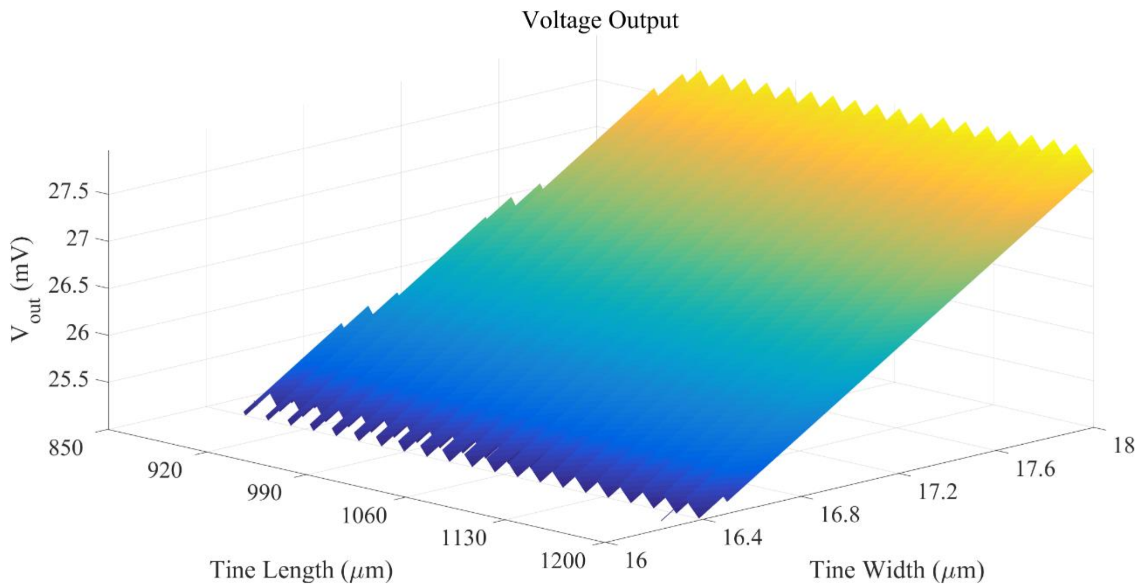

Figure 3.8 - Surface plot of voltage output function which is a limiting factor the design

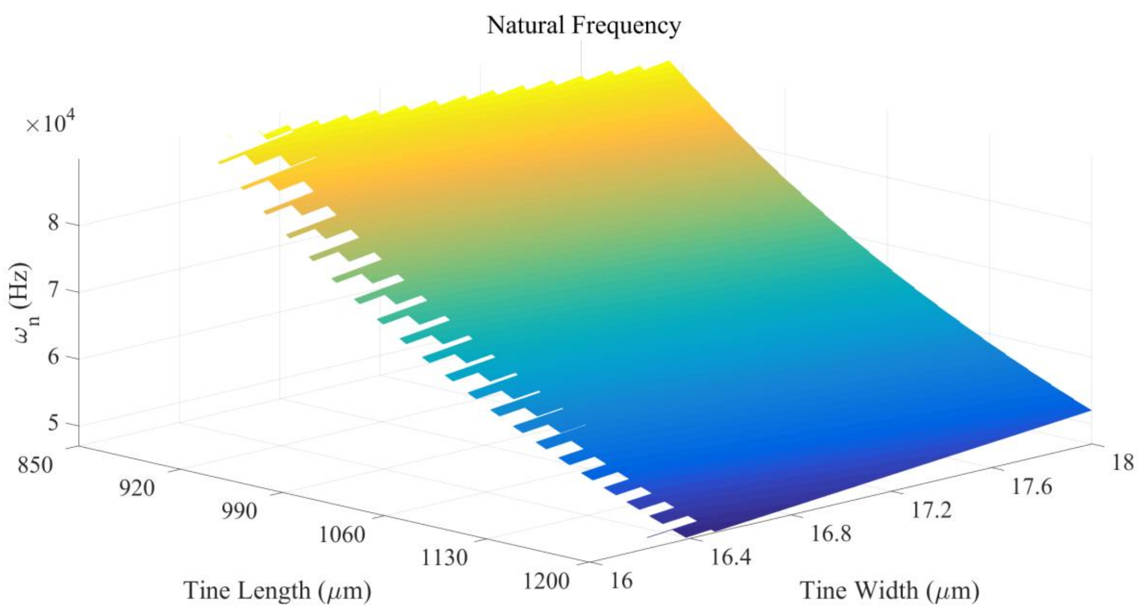

Figure 3.9 - Surface plot of natural frequency function which is a limiting factor the design

Following two figures belong to factors which are used for choosing the design, namely sensitivity and quality factor functions, respectively. Note that sensitivity is calculated for a DETF without a spring and given with unit of Hz/m.

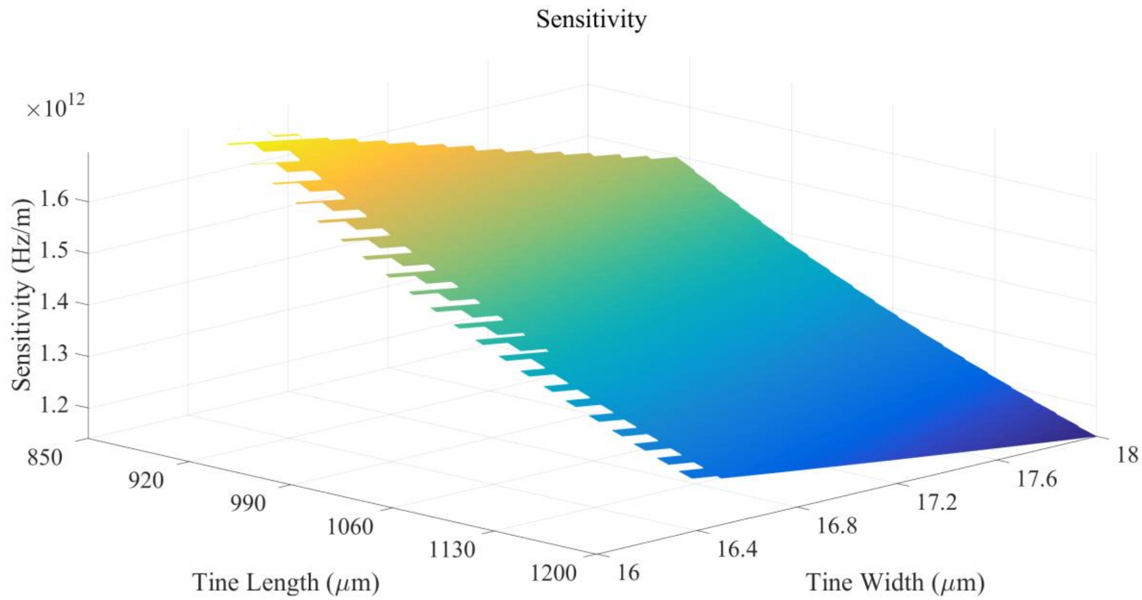

Figure 3.10 - Surface plot of only sensitivity function for all device designs which can satisfy natural frequency and voltage output limits within specified boundaries

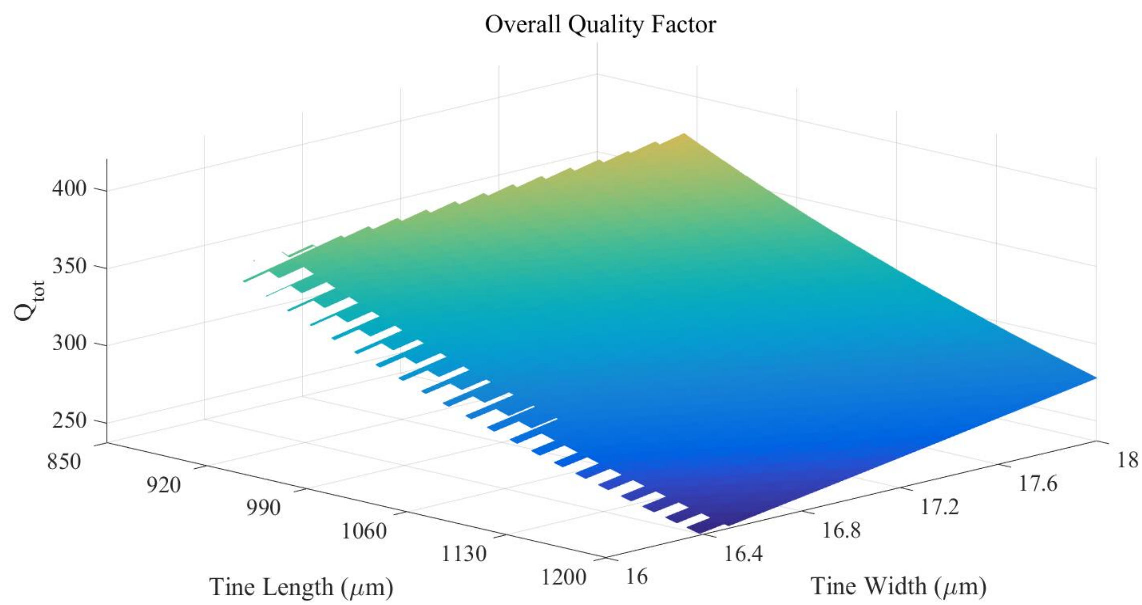

Figure 3.11 - Surface plot of only quality factor function for all device designs which can satisfy natural frequency and voltage output limits within specified boundaries

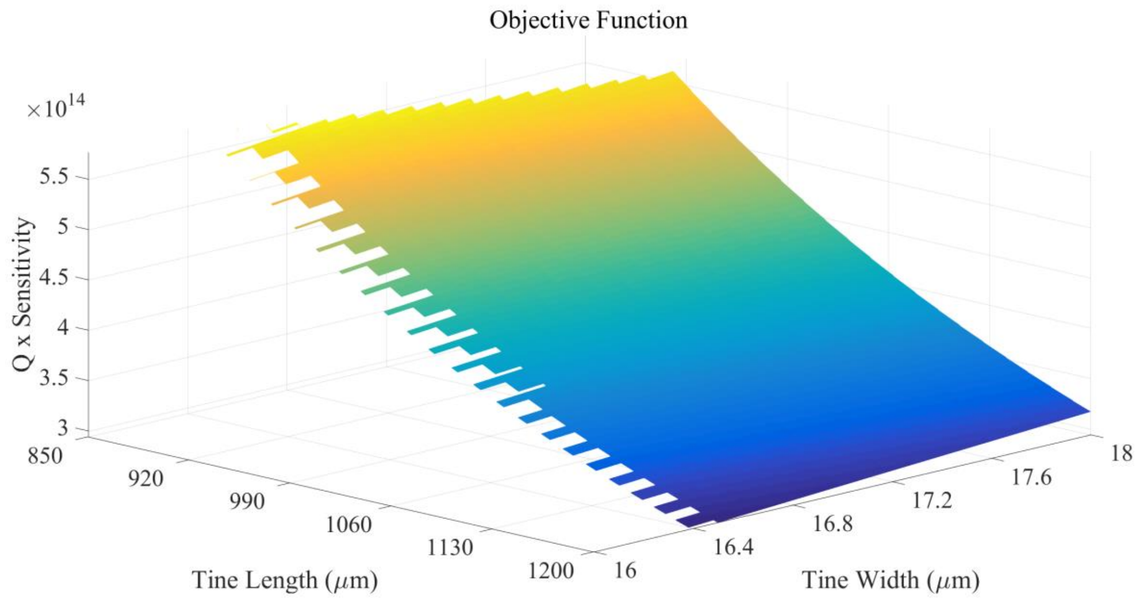

Figure 3.12 - Surface plot of objective function belonging to all device designs which can satisfy natural frequency and voltage output limits within specified boundaries

Finally optimization routine multiplies sensitivity and quality factor and obtains a value of which unit is simply Hz/m. Then picks the maximum value of this function and prints the corresponding dimensions. This maximum value and corresponding dimensions can be read from top left corner of the plot from Figure 3.12.

3.2.4. Numerical Verifications

In this section results of finite element analysis are presented. The results include tabular comparison of uncompressed natural frequencies found with single degree of freedom model and COMSOL MEMS Module. Moreover, the same comparison is made for buckling analysis. Lastly, the first 8 mode shapes of a design are shared.

Table 3.3 - Natural frequency and percent accuracy of it when found by theoretical model and finite element analysis

SDOF Model		COMSOL
89.99 kHz	14.0%	78.95 kHz

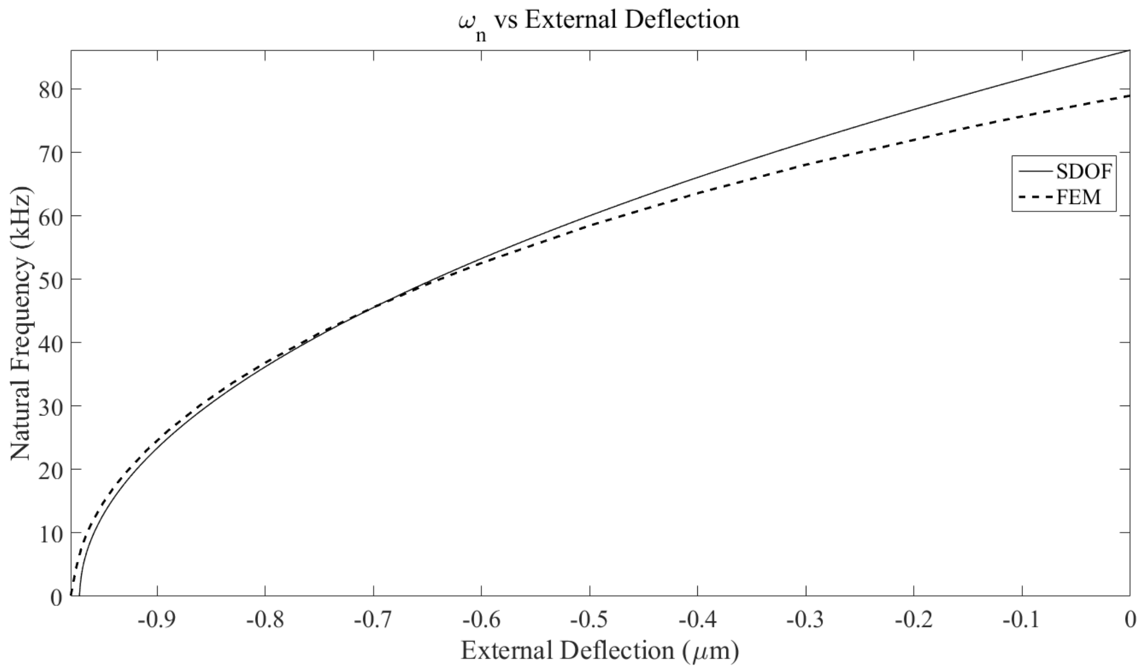

Figure 3.13 - Comparison of numerical and theoretical solutions on axial loading vs natural frequency graph for Design 1

The length of capacitive plates are set to be equal to 90 % of length of the tines which is actually a value such that it can cause non-linearity. And hence since capacitive plates are assumed to be rigid in the model, a difference was expected between single degree of freedom model and simulation results. But it is seen from Figure 3.13 that the point at which theoretical model is apart from simulation results the most is zero deflection point. When loading starts model converges and becomes more accurate. Therefore it can be stated that single degree of freedom model is acceptable for this optimization.

The first 8 mode shapes of DETF with comb finger configuration capacitive plates are illustrated in Figure 3.14. Significance in this figure is that out of plane modes are well separated from desired mode shape. Moreover it is important that desired mode shape has to interfere with only two in-plane modes while loading i.e. when the frequency is decreasing.

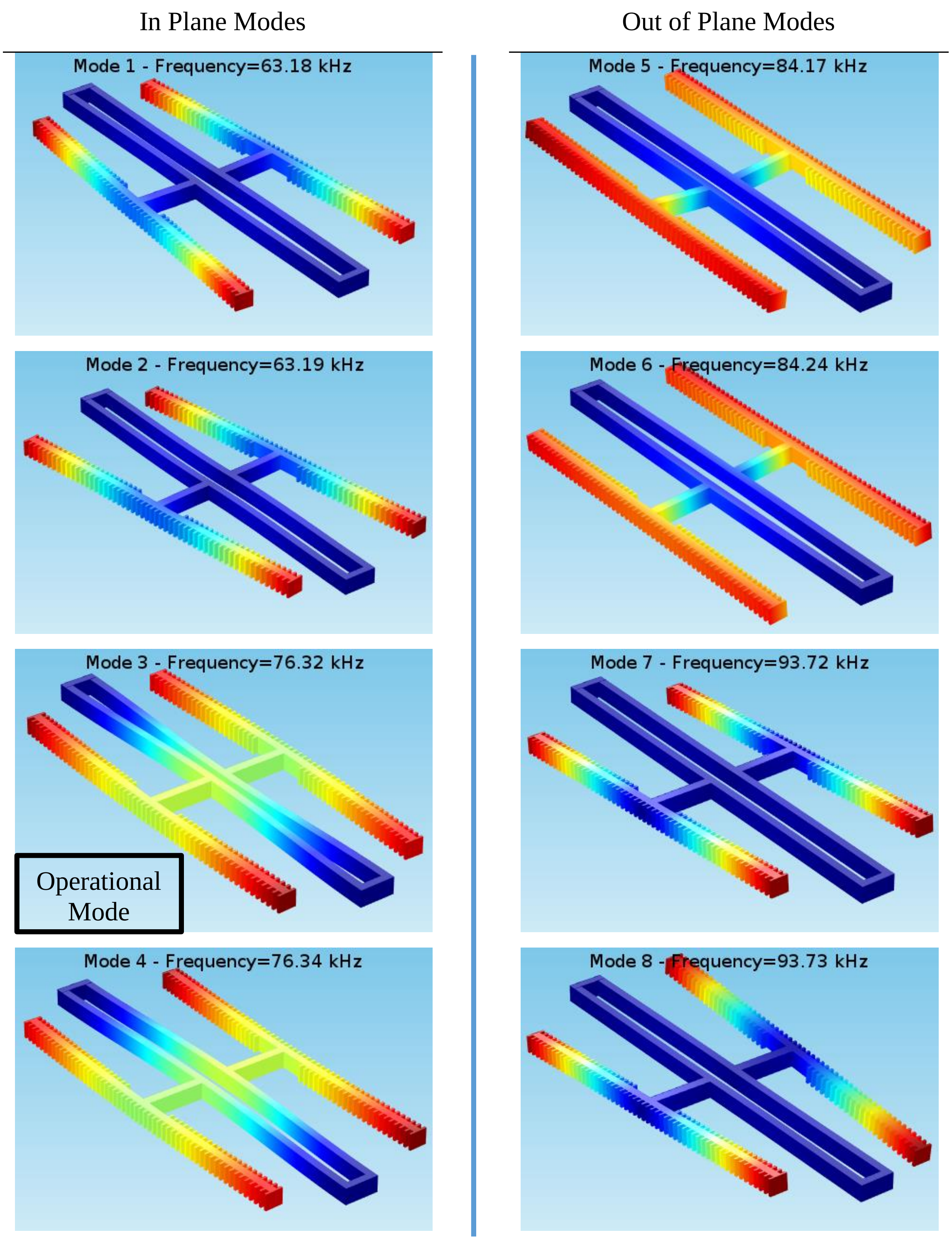

Figure 3.14 - The first 8 mode shapes of DETF with corresponding natural frequencies and order. In plane and out of plane modes are well separated and they are shown in separate columns

3.3. *Design of Supplementary Structures*

While introducing the ideas of the design, a spring and a roller element was introduced in the beginning of Section 3.2. Also illustrative view of these supplementary elements along with their junction points to each other and tuning fork was given in Figure 3.2.

Purpose of these additions was also mentioned before in context as protecting the device. Spring has to absorb 100 µm of deflection while transmitting only around 1 µm to DETF since buckling for DETF alone occurs at 1 µm which can be seen from Figure 3.13. Actually the objective of adding a spring to design is to expand x axis of curve in this figure up to 100 µm. And roller element is added in order to eliminate the effect of transverse components of loading.

The main problem with this elements is 100 µm is a very large deflection to handle. It is decided that simulating the effect of such deflection is necessary for defining geometry of springs. By using COMSOL Multiphysics MEMS Module, deflection and stress analysis is conducted and dimensions of the elements shown in Figure 3.2 are found. Another point in choosing simulations for analysis is that both of these elements are susceptible to 100 µm deflection and it is possible to see the effect of loading on spring and roller simultaneously in simulations. Analytical methods are not addressed for this part of the design because simulations was enough and straightforward.

An effective arrangement of device elements is essential for microfabrication because it can be also related with yield. Thus it is chosen to use a spring which comprised of 2 large folded beams for handling 100 µm of deflection as available space for one sensor promoted. Roller element is attached to the spring structure allowing only axial loads to reach to it. It is composed of 4 folded beams which are supported by 4 additional one side anchored beams in the middle. Constraint for definition of this spring element is the yield strength of silicon which is around 7 GPa [1]. But to be on the safe side, maximum stress is kept under 1 GPa.

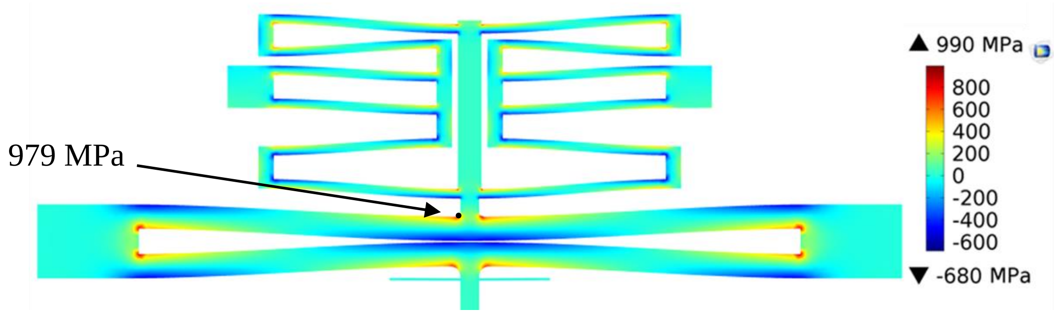

Figure 3.15 - Deformation of supplementary elements under 103.5 µm of axial tip displacement. Point of maximum compressive stress is shown. DETF in the model is not shown for salience.

After addition of roller and spring to the structure, it is found out by simulations that natural frequency of the device is shifted a little and became 79.48 kHz. In theory there should be no difference because the supplementary structures are not in motion at desired mode shape. But, in reality tines apply harmonic forcing to the spring element and hence they interfere with desired mode also. Due to that reason a little shift is expected.

A screen capture from FEM package is given Figure 3.15 including the point of maximum compressive stress and corresponding value. As expected this maximum stress point is positioned at the junction point of beams of roller where fillet at the corner is the smallest in radius. Corresponding geometry is also illustrated in Figure 3.16 with dimensions.

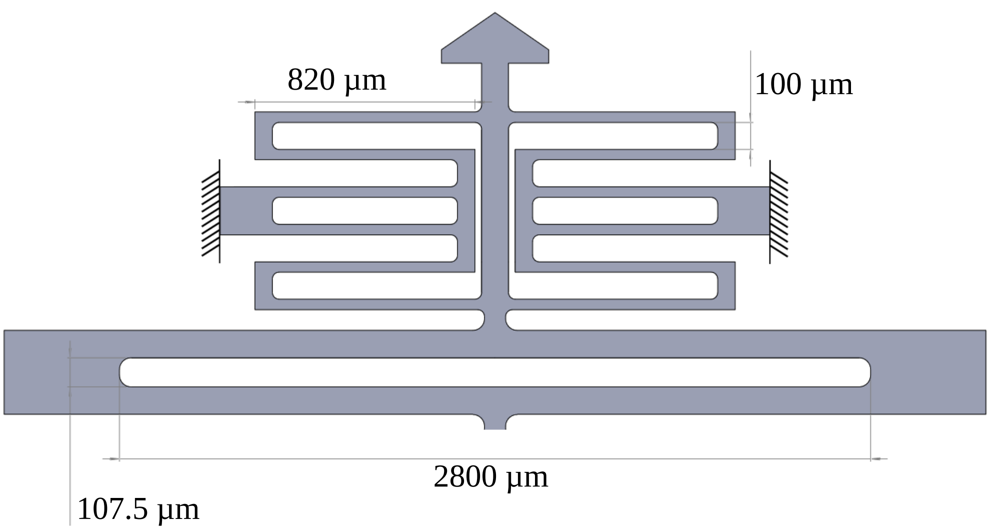

Figure 3.16 - Drawing of spring and roller elements with important dimensions

3.4. *Summary*

Detailed design of the sensor is presented by dividing the design into three sections. In the first section, design of package is explained with necessary safety calculations. These include calculation of safety factors for diaphragm and fastener. The second section describes optimization of the resonator structure. Specifically, objective function, design parameters, design constraints and assumptions are defined and calculations of mechanical and electrical properties are demonstrated. These properties include, resonance frequency, sensitivity, voltage output, quality factor and resolution of the sensor. In addition, results of optimization code are validated with numerical findings. In the last section, designs of supplementary structures are presented with their objectives and numerical analysis.

CHAPTER 4

FABRICATION

In this chapter fabrication of the proposed sensor is explained. Process flow has 2 step fabrication, surface microfabrication of MEMS sensory part which involves several cleanroom processes and a manufacturing of pressure port for which few basic conventional machining techniques are sufficient. This section begins by explaining conventional machining sequence of pressure port which took place in METU Mechanical Engineering Department Machine Shop. Secondly, main processes of surface micromachining are presented.

4.1. Manufacturing of Pressure Port

First restraint for pressure port of the design has to be applicable to hydraulic test setup. Thus, Bosch Rexroth Hydraulic pressure setup which is available at METU Mechanical Engineering Department Automotive Laboratory is investigated and proper pressure port geometry is defined. Pressure port is composed of 2 different materials. Aluminum is utilized for its better yielding properties in diaphragm part, whereas steel is used for its superior strength at threaded part.

Both of these parts are machined in conventional turning machine with a precision of $\pm 0.1\ mm$. Then these parts are fixed to each other with an interference fit. The interference fit is obtained with 100 µm of interference and fitting two parts by using a clamp.

As a supplementary part, a brass cylinder is assembled to the pressure port in order to slide the sensor board in. This part is combined with the structure with fitting but this time it was a loose fitting in order to be able to replace it later. Finally obtained pressure port is shown is shown in Figure 4.1.

Obtained pressure port has diaphragm thickness of 1 mm due manufacturing capabilities although the design proposed 0.72 mm for a safety factor of 2. This decreases sensitivity further nonetheless it is acceptable in order to prove the concept.

Figure 4.1 - Picture of a manufactured pressure port

4.2. Fabrication of MEMS Sensor

Fabrication flow shown in Figure 4.3 starts with a <100> type SOI wafer in order to have superior device characteristics while keeping the device layer insulated and requires only 3 masks. The SOI wafer used in this fabrication has a device layer thickness of 35 µm and handle layer thickness of 350 µm. The buried oxide layer thickness is 2 µm. Although it is started with a brand new wafer, piranha etch takes place in order to get rid of any residue of production processes such as chemical metal polishing. The second step of the processes is to coat 0.7 µm of Cr/Au as a metal layer in sputter with thicknesses of 30 and 300 nm, respectively. Then metal layer is patterned in wet etch to obtain connection pads for electrodes of the structure. After metal patterning, device layer is etched in DRIE.

Device layer is 35 µm and this layer is little over etched. Then in the fifth step, it is required to etch the handle layer in the same manner in order to be able release the vibratory parts of the structure. As a mask to handle layer etch, 0.5 µm of PECVD oxide is coated on the backside. However, arising problem with handle layer etch is, after using DRIE on one side it is difficult to apply patterning on the opposite side because of the ducts which are opened on this surface. These ducts prevents vacuum holder of spinner and aligner equipment from holding the wafer properly. Therefore a dummy glass wafer is made use of for binding the wafers together for lithography. Photoresist of the same type is used for binding. After binding, glass wafer is vacuumed by spinner and handle layer is spin coated carefully and backside pattern is applied. Then RIE of backside oxide mask takes place, afterwards handle layer is etched with DRIE.

Finally following the last DRIE process, fabrication proceeds with the 6th step which is RIE. In this step buried layer of oxide is stripped using silicon as masking layer. But instead of this BHF solution can also be applied to release the structures.

Devices are directly ready for operation after this last microfabrication process because subtraction of devices does not require dicing. In the design phase, devices are connected to branches which are preserved through the process. One example view of these branches on the mask which is used for handle layer etch is shown in Figure 4.2. Note that this is a dark field mask and positive photoresist is used at coating, these devices can easily get ripped apart from the branches like a fruit. Moreover, for ease and regularity, branches are indented at desired locations. These indents are to initialize the crack while breaking and prevents cracks from propagating improperly.

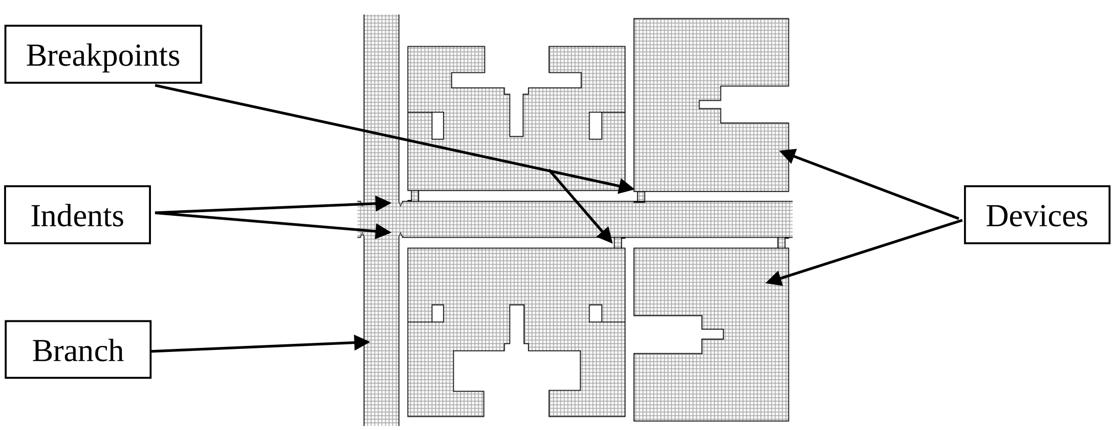

Figure 4.2 - Example of a layout drawing view of one of the braches to which devices are connected.

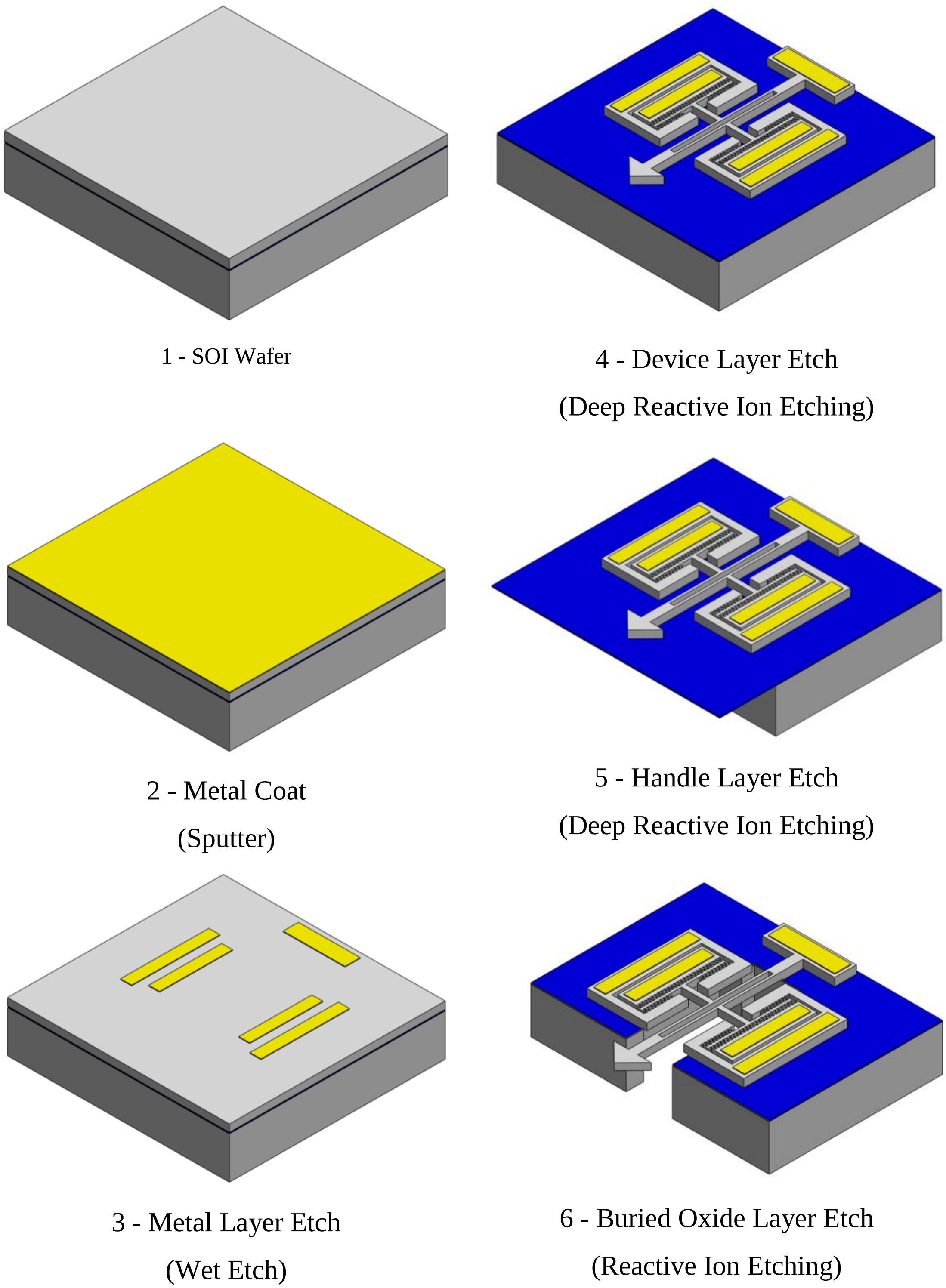

Figure 4.3 - 3D illustration of fabrication process steps of resonator. Blue and yellow colors represents oxide and gold, respectively while the grey layers are single crystal silicon.

Keeping in mind, fabrication being a very complex procedure, it is very difficult to optimize and standardize it. It is possible to go through each step very intensively and optimize the fabrication for the highest yield but in this study very few done for such purpose. Standardizing this process can be another study therefore fabrication steps are only briefly explained up to this point and any further detail is not given.

Scanning electron microscope photos of devices are shown in Figure 4.4 and Figure 4.5. Objective of these figures is to illustrate spring and roller elements and tuning fork resonator. For that purpose a close-up image of DETF is shown in the first image and in the next image all three active elements of the device is captured.

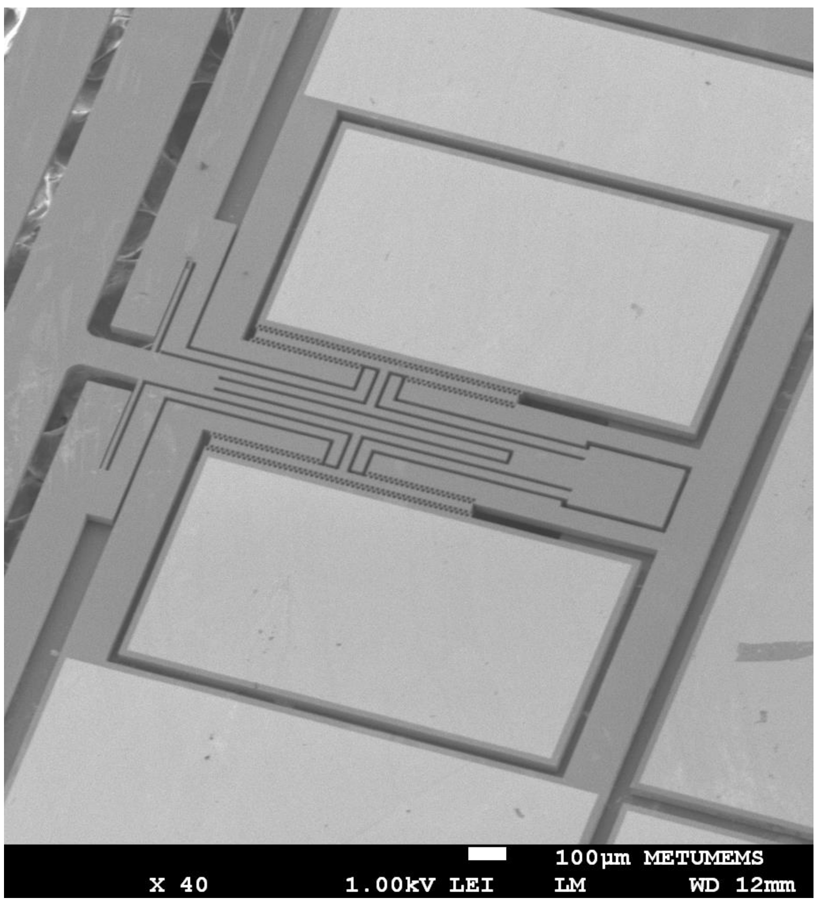

Figure 4.4 - Close-up SEM image of 867 µm long DETF along with its connection point with spring element and anchor

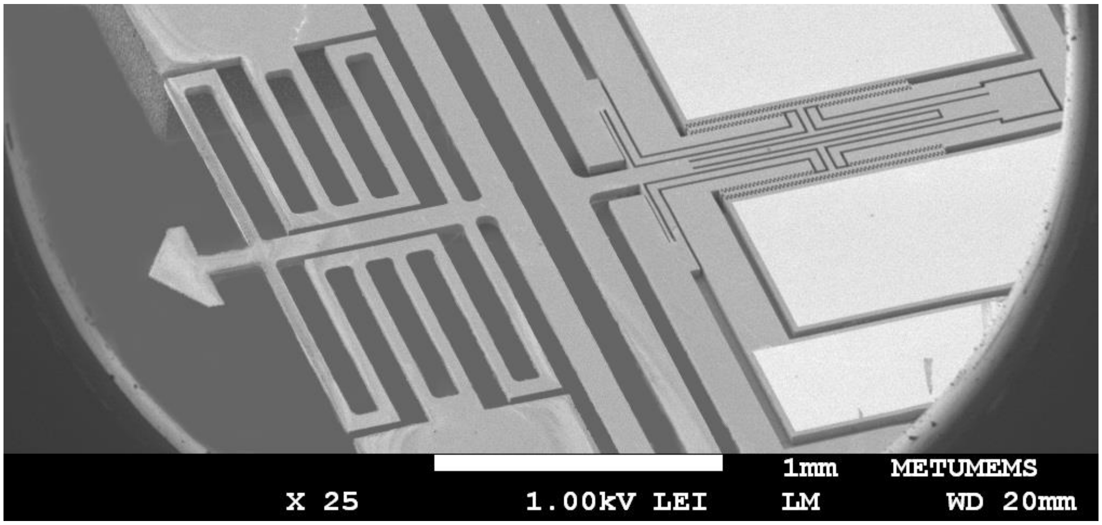

Figure 4.5 - Wide view of tip, roller, spring and tuning fork with SEM

4.3. Summary

Details of the fabrication of the sensors are presented. First manufacturing of pressure port element is described. This element is machined in a conventional turning machine. Secondly, the cleanroom processes are explained along with the related design considerations. In order to enhance description of processes, 3 dimensional illustration of microfabrication steps are given. Lastly, the scanning electron microscope photos of the obtained devices are shown.

CHAPTER 5

CHARACTERIZATION

After fabrication, devices are tested for their resonant properties one-by-one. In this section procedure of characterization and relevant results are shared. Also in the flow of context, assembly of the device is explained before hydraulic pressure test.

Tests can be discussed in mainly 3 different categories. These are;

1. Resonance test
2. Displacement test
3. Hydraulic pressure test

The objective of the first step is to determine whether the subject device is working properly or not. Then displacement tests took place to see the performance of device under axial loading. Sensitivity of the device is calculated from the result of displacement test response of device is investigated. Then in final step of tests, sensor body is assembled and device is tested on real operation.

5.1. Detection Scheme

As mentioned in introduction chapter, digitizing the output of a resistor is rather easier. Detection scheme shown in Figure 5.1 is only consists of a power supply, network analyzer and a trans-impedance amplifier. Purpose of power supply is to provide DC voltage for proof mass. This is the voltage which creates capacitance across sense electrodes and the resonating mass. Network analyzer is used for driving the structure to resonance. Basically AC drive voltage is fed to drive electrodes by network analyzer in a certain frequency interval while output voltage is also collected by it. Consequently, frequency response of resonator is obtained.

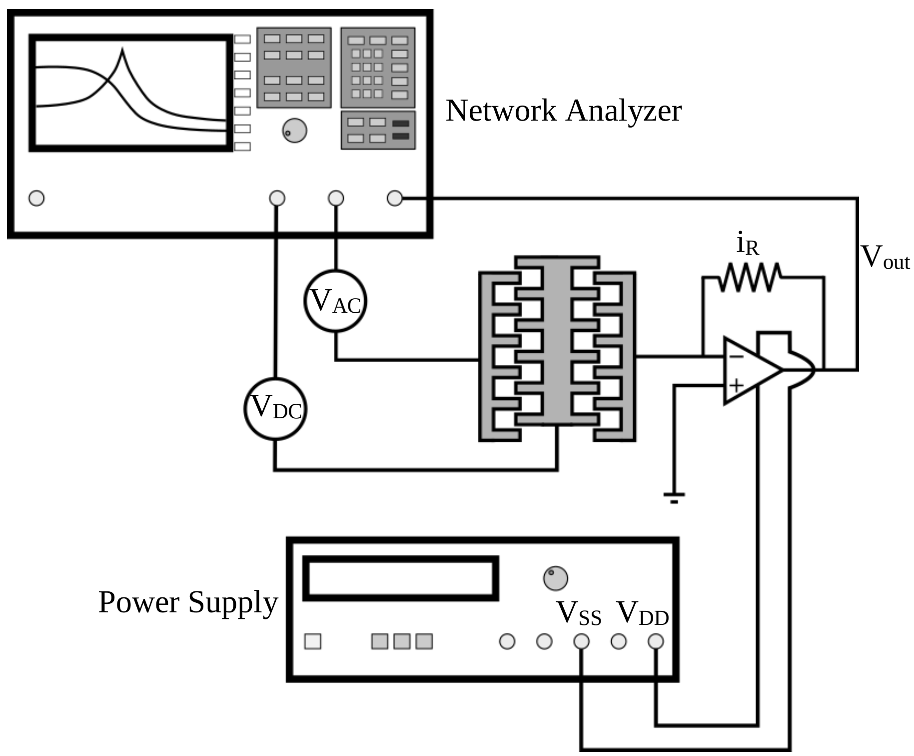

Figure 5.1 - Schematic drawing of detection setup consisting of a network analyzer, DC power supply, resonator and trans-impedance amplifier.

Instead of current output voltage is preferred form of output because it is easier to handle. It can be fed into network analyzer which compares drive and sense signals directly to obtain frequency response. Essential reason for presence of trans-impedance amplifier is the need for converting current into voltage. Output current rises from alternating capacitance between sense electrode and proof mass. This current is then converted into voltage with help of an operational amplifier and a resistance named as gain. The conversion is discussed later in design chapter while computing output voltage.

The above shown detection method is one of the simplest ways of detecting natural frequency of a resonator. However, in this method the natural frequency is found by scanning a frequency interval. For the proposed sensor, it is suggested that application of pressure changes natural frequency. Hence at every different pressure value, scanning takes place which apparently is costly in terms of time. Therefore improved methods consisting of electrical circuits are implemented such as self-resonance and phase-lock loop. These are superior closed loop natural frequency detection methods used to drive the resonator at resonance always. But this type of measurement is also enough for this study since it is not possible to detect the pressure of hydraulic fluid inside electronically due to conditions of setup. However it might be a good merit if the resolution of the sensor was measured. Therefore using these closed loop resonance circuits and measuring minimum detectable pressure is left as a future work.

5.2. Resonance Tests

All dies are subjected to this first test using the equipment shown in Figure 5.2and the circuit which can be referred from Figure 3.6. Moreover whole scheme of the setup can be seen in Figure 5.1. During resonance tests, sensors were not mounted onto a package surface and the electrical connections were not taken out yet. Hence, connection between the electrodes of MEMS and the setup is obtained using a probe station.

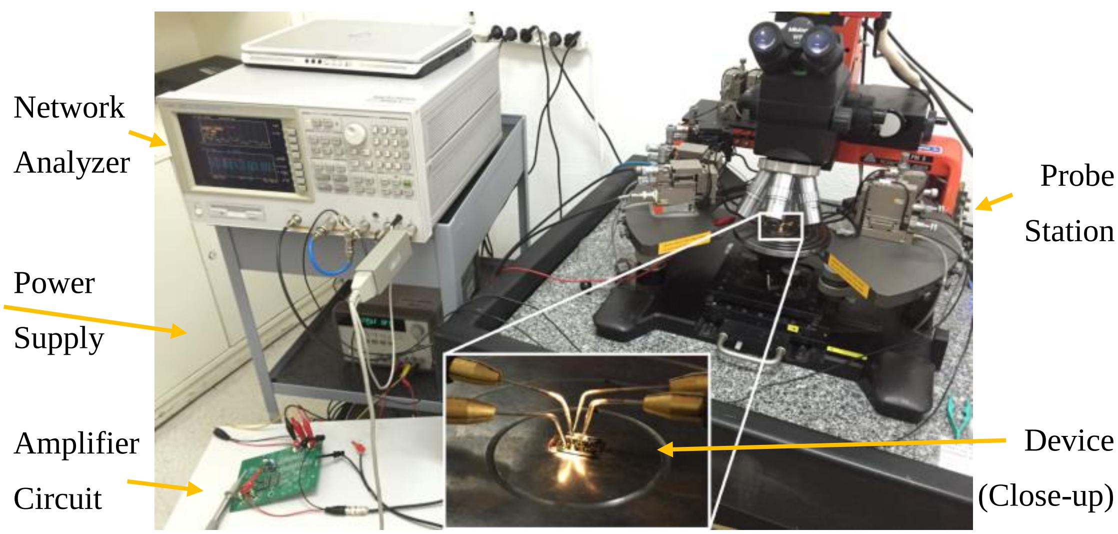

Figure 5.2 - Picture of test setup, network analyzer, power supply, probe station and sensor.

The configuration of network analyzer shall be presented for coherence. First of all, model of the equipment is Agilent 4395A Network Analyzer. Sensors are driven to resonance with AC signal having a power of 15 dBm watts. DC voltage is fed to proof mass by network analyzer and set to 40 V. IF bandwidth setting for measurements is configured to 30 Hz and sweeps are taken at 801 points. It is paid attention to have a greater interval of frequency than IF bandwidth between each data point.

In these tests, quality factor values up to 260 are observed. This is due to atmospheric operation conditions but low quality factor drastically affects the results. Yet 2 of the corresponding results are demonstrated in Figure 5.3 and Figure 5.4. The first figure represents the frequency response of a sensor which is operated symmetrically. This means that, it is driven using 2 drive motion is sensed through 2 sense electrodes. Whereas the second figure belongs to a sensor which was operated by 1 drive and 1 sense electrodes which causes asymmetrical operation. Therefore it is expected to see more than one peak in the frequency response. The reason that the latter is driven as such is probably a dust particle which connected two of electrodes accidentally and disabled those electrodes. Vulnerability to dust is mainly due to non-enclosed sensor design.

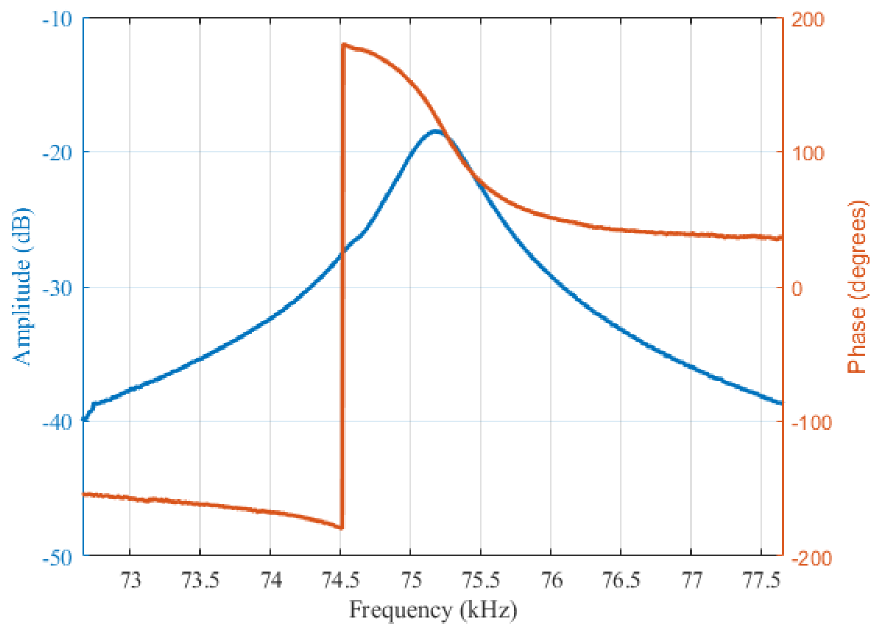

Figure 5.3 - Frequency response of a sensor which has a quality factor of 158. Note that jump in the phase curve is due to reaching -180 degrees

In the second result, 2 fused peaks are observed which is mainly due to aforementioned asymmetric drive conditions. And even there is a small peak on the left around 72 kHz.

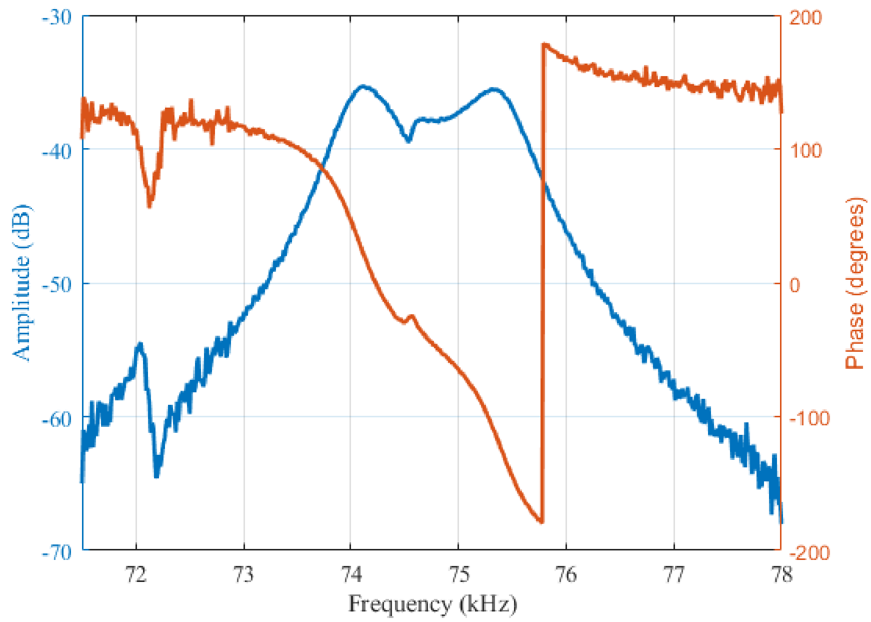

Figure 5.4 - Frequency response of a sensor driven by only 1 electrode asymmetrically. Q values related with peaks are 134 and 75, respectively.

5.3. Displacement Tests

Displacement tests are conducted for one of the sensors. Sensors are fixed on to the surface of the probe station table with vacuum, and a metal part is fixed at the back of the sensor to make sure that it is fixed well. This configuration is shown in Figure 5.5Also in this picture piezoelectric actuator can be seen with the metal part mounted on to it in order to aim the tip of device.

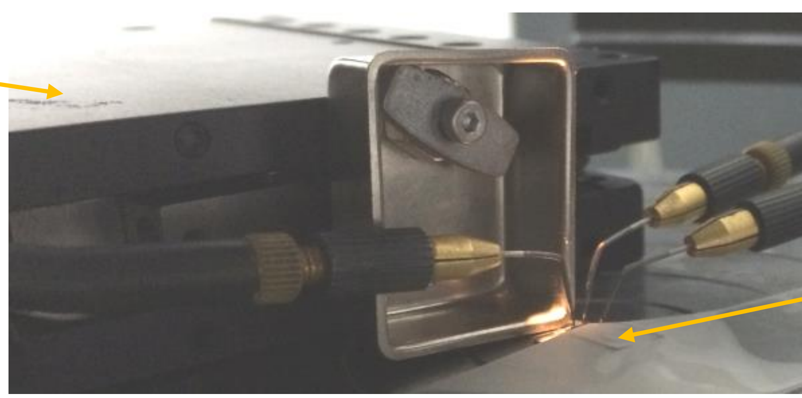

Figure 5.5 - Additional equipment for displacement test setup and fixing of the sensor. Sensor tip is deflected with piezoelectric actuator's upper half with the help of additional metal parts.

The piezoelectric actuator's minimum incremental linear motion with power supply used is around 3.3 nm/mV which is sufficient for tests. During tests measurements are taken at every 1 V change for 25 V range and every 2 V for 50 V range, which corresponds to 6.6 μm of deflection. In the following figures results of 25 V and 50 V scale tests are shared. It should be noted that, tests do not start from 0 deflection, rather than that, actuator is placed very closely to tip under microscope with no contact. Test starts when frequency shift is observed with increasing actuation voltage. For the first result starting voltage is found experimentally as 11 V but this is not precisely known. Whereas for the second test starting value is estimated to be around 12.86 V. This value is estimated by interpolation. Comparing the amounts of frequency shift occurred with the first and second increasing step of voltage yields this value.

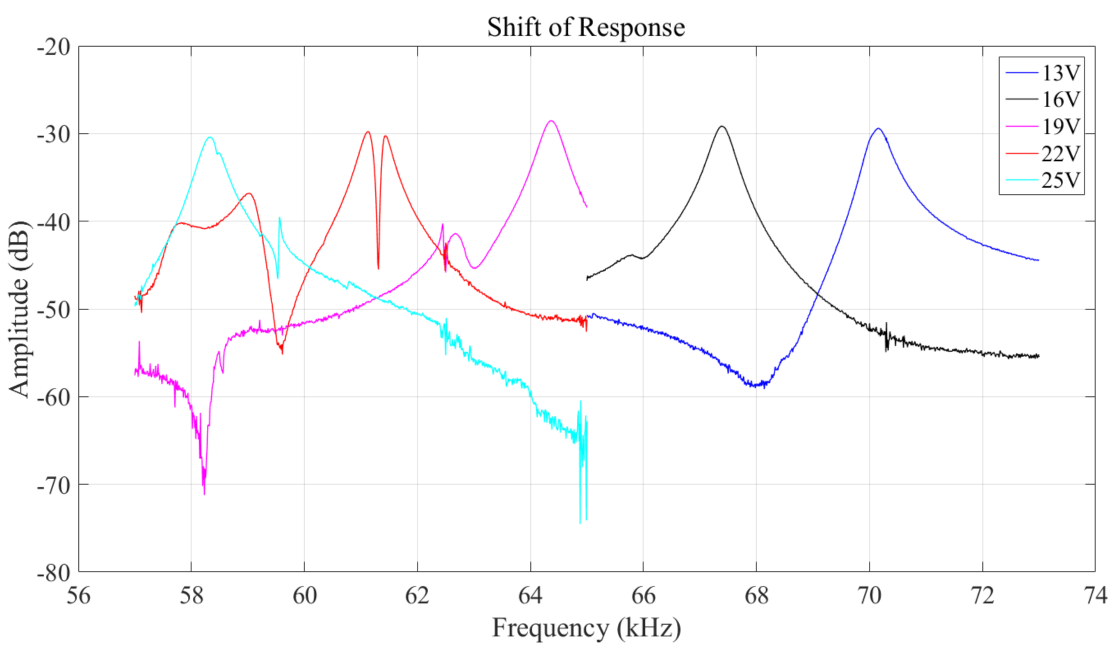

Figure 5.6 - Resulting responses from the first loading with a scale of 25 V actuation voltage. Note that shift started at around 11 V.

In Figure 5.6 responses of device under different loading conditions are illustrated. Voltage scale of the test was 25 V. After this test it is seen than the scale can be increased. Results of test with wider scale are given in Figure 5.7.

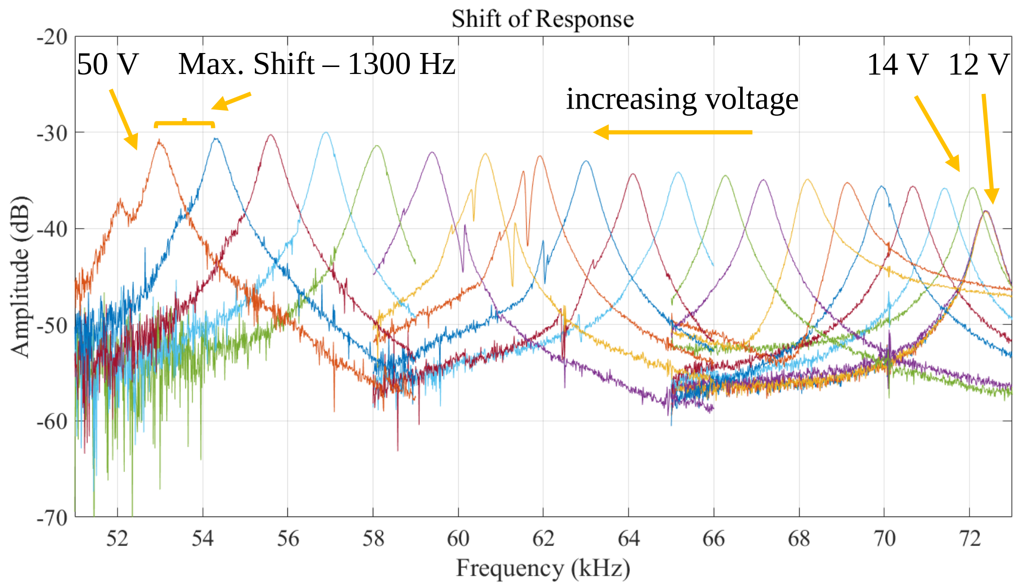

Figure 5.7 - Frequency response curves when the voltage is increased to 50 V. Note that step increase in piezoelectric actuation voltage is 2 V

Maximum shift is occurred at the end of scale as being 0.65 kHz/V while the minima is collected at the beginning between 14 V and 16 V as 0.34 kHz/V. Without a break, this test is repeated in reverse order. Corresponding results are also shown in Figure 5.8.

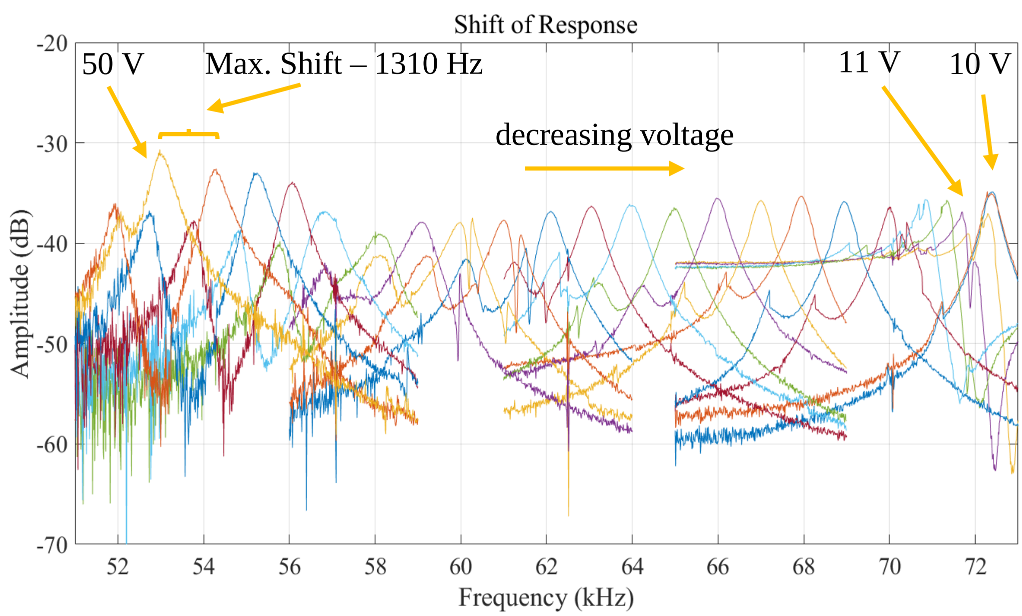

Figure 5.8 - Frequency response curves when the voltage is decreased from 50 V. Note that step increase in piezoelectric actuation voltage is 2 V

In unloading tests actuation voltage is decreased from 50 V by 2 V step decrease until the tip is freed. It is seen that this time tip returned to its initial condition between 10 V and 11 V. Interpolation gives a release voltage of 10.31 V. However starting voltage was estimated to be 12.86 V. This was expected because even though the setup is fixed as good as it gets, position change is inevitable.

Natural frequencies obtained from Figure 5.7 with corresponding actuation voltages are given Figure 5.9 for better comprehensibility.

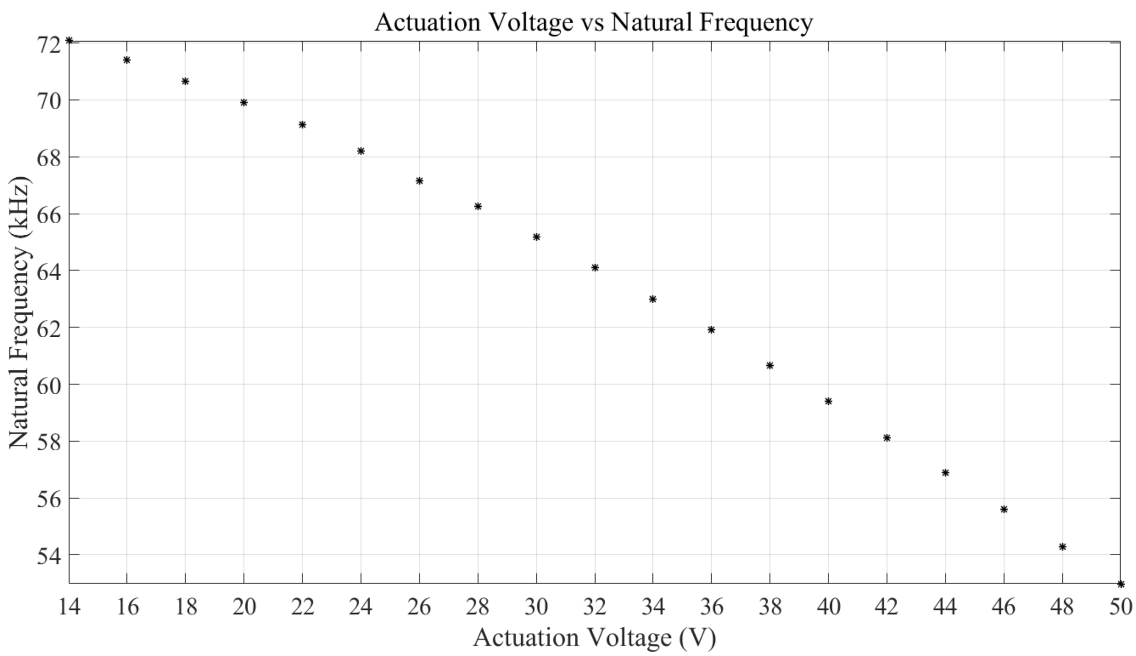

Figure 5.9 - Graphical illustration of the results of the second displacement test

Maximum sensitivity in displacement tests is obtained as 198.49 Hz/µm. knowing that 1 mm thick diaphragm is deflected at the center for 1 µm under 21 Bars, the sensitivity is equivalent of 9.45 Hz/Bar.

5.4. Assembly of Device

Before assembly of the device, a board is prepared for sensor to sit on. A tiny copper board with dimensions 5.96 mm x 20 mm x 1.5 mm is cut for that purpose. After electrical connections are created on the board, cables are soldered. There are 5 cables coming out from the board 3 being drive, sense and proof mass connections and the remaining 2 being ground in between. The ground electrodes are meant to decrease interference between drive, proof mass and sense signals. Then MEMS sensor is placed. The contact between board and sensor is established via silver epoxy. Then electrical connections are taken out to the copper board from sensors electrodes. Finally, sensor is placed in metal cylinder which will fit into pressure port. A picture of this first foundation is given in Figure 5.10. At this point tip alignment is very important. Due to fillets on the edge of diaphragm, tip has to reach out from the cylinder for another 250 µm to ensure its connection with diaphragm. Corresponding microscope view can be seen in Figure 5.11.

Figure 5.10 - Close up view of a sensor inside the cylinder with its electrical connections completed.

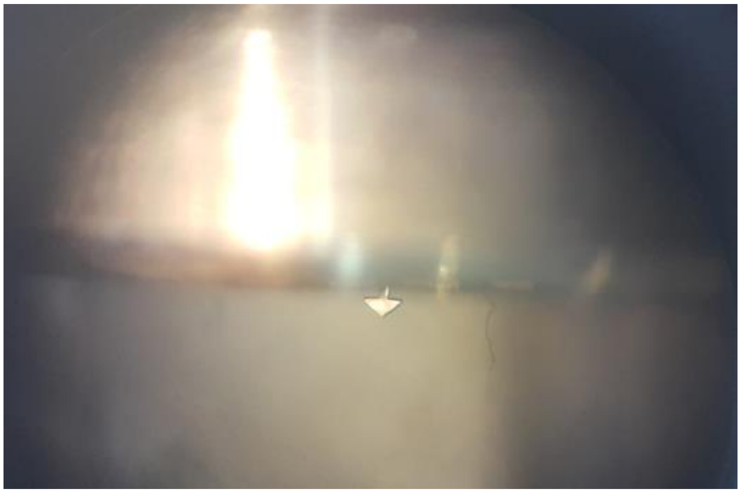

Figure 5.11 - Microscope view of tip left out of the cylinder. Approximately 250 µm of it is out as desired.

After the board is fixed to cylinder with epoxy, it is enclosed by pressure port and tested. When a 1 kHz of shift is observed in it frequency response, finally it got fixed all with again epoxy. This shift can be seen in the following figure.

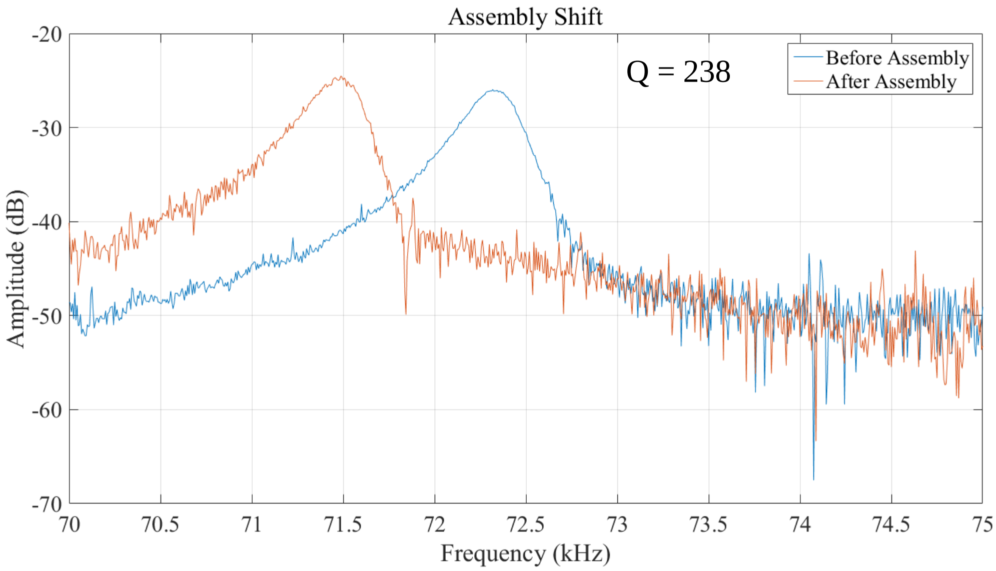

Figure 5.12 - Illustration of frequency shift occurred during assembly which ensures that tip is in contact.

Final view of the device is given in Figure 5.13

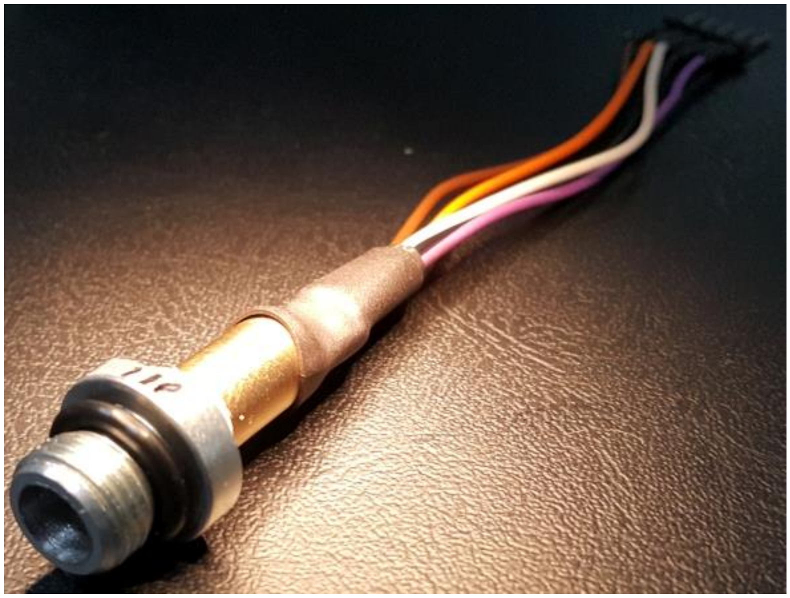

Figure 5.13 - Assembled view of the hydraulic pressure sensor.

5.5. Hydraulic Pressure Tests

Texas Instrument's low cost op-amp LF-353 is used throughout resonance tests. It should be mentioned that this amplifiers noise properties are used in design optimization. But only after MEMS sensor is placed onto a circuit board, this amplifier became insufficient in terms of its noise properties. Then again Texas Instrument's low noise, surface mount op-amp which also has a wider band, OPA-656 is employed. Trans-impedance amplifier circuit for OPA-656 requires a little bit modification as it need capacitances between power pins for operation. Thanks to Mustafa Kangul, this circuit was readily available for use and directly adopted.

Hydraulic pressure tests are conducted at METU Mechanical Engineering Department Automotive Laboratory. Picture of the setup is shown in Figure 5.14. Threaded portion of pressure port is designed in order to fit the hydraulic equipment in the laboratory. Test equipment is able to apply a pressure of 50 Bars with losses included. The pressure values are measured in advance at the same point where the device is placed to be exact.

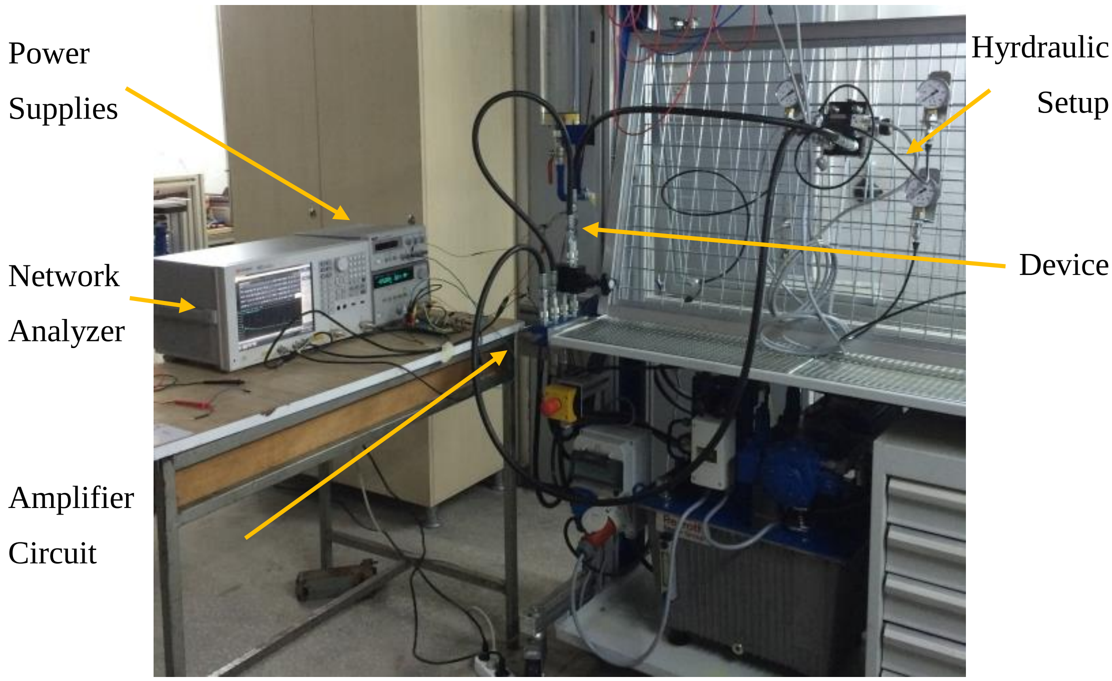

Figure 5.14 - Picture of hydraulic pressure test setup

Tests data is collected for 5 pressure points up to 50 Bars. This time resonance peak cannot dominate noise level well. There are 2 main reasons of this. First, test are carried out with a proof mass voltage of 15 and 24 V. Remembering that the previous tests were conducted with 40 V, a smaller resonance peaks are expected. Secondly, active probe which was available for displacement tests were not present in the setup. When an active probe is utilized for the transmitting output voltage signal to the system, resonance peaks are well observed and noise level is suppressed. Frequency response of the device at applied pressure range of 0 - 50 Bars is demonstrated in following figures. 6 responses which belong to 6 different data points, are given separately because it can be very difficult to decompose them in one figure because of noise level.

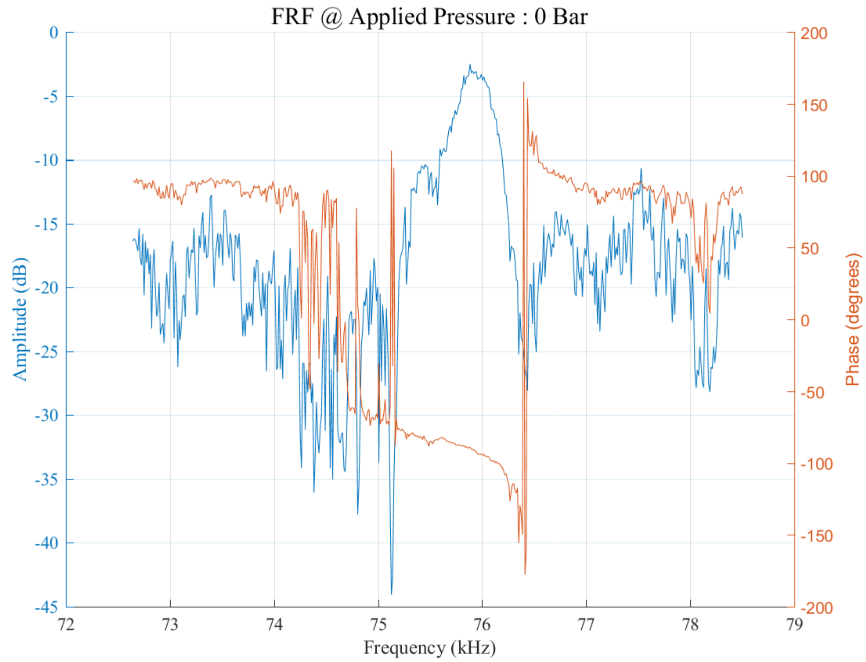

Figure 5.15 - Frequency response of the device with no applied pressure

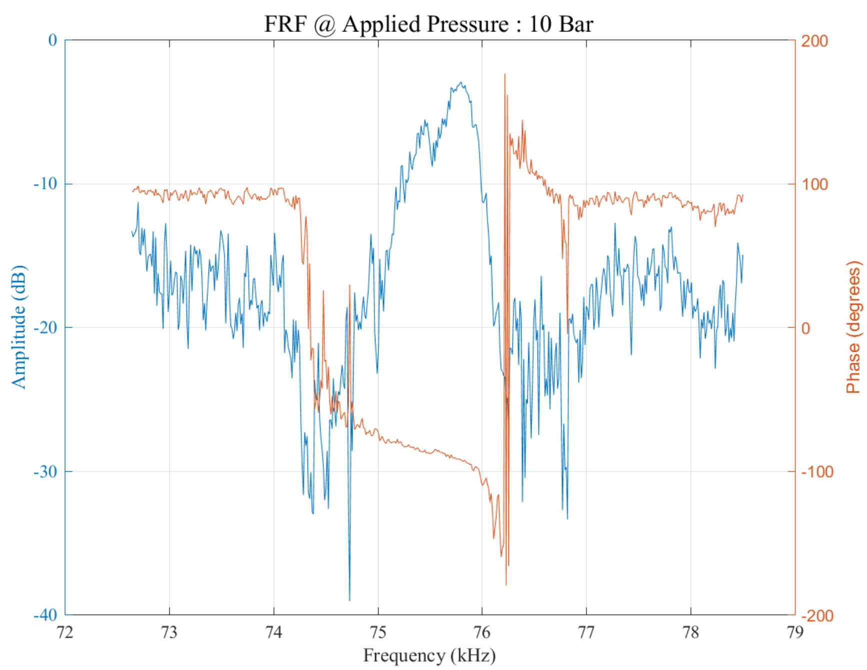

Figure 5.16 - Frequency response of the device at 10 Bars of applied pressure

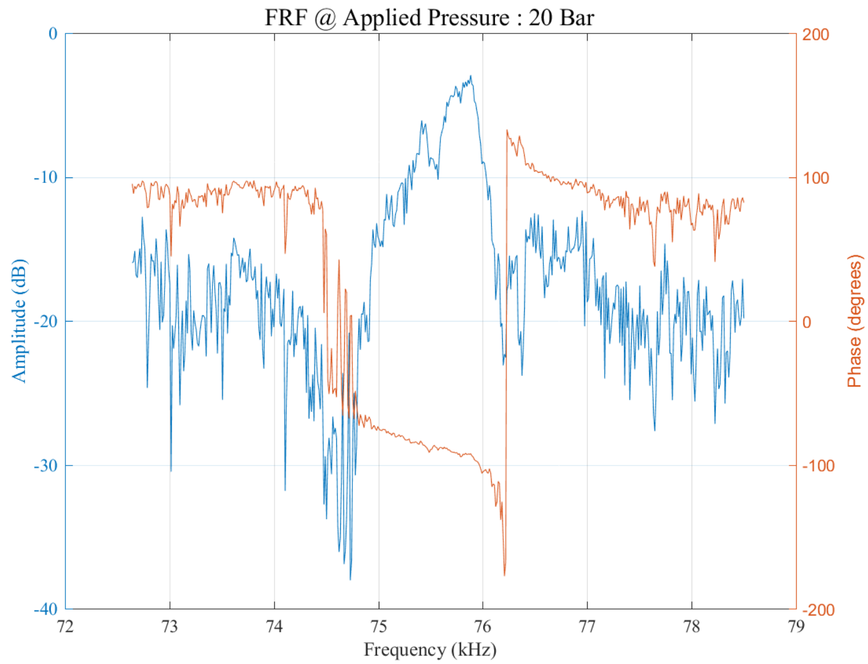

Figure 5.17 - Frequency response of the device at 20 Bars of applied pressure

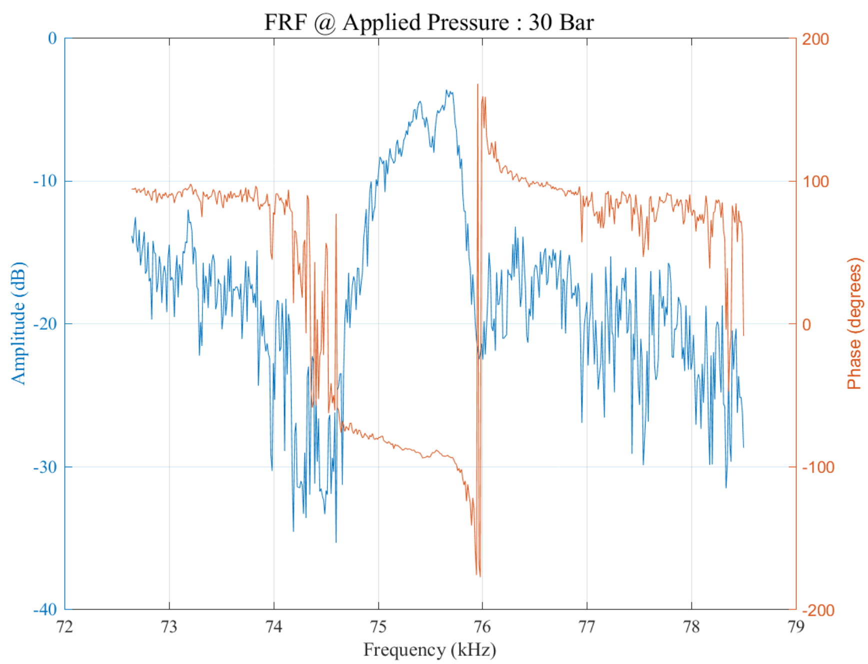

Figure 5.18 - Frequency response of the device at 30 Bars of applied pressure

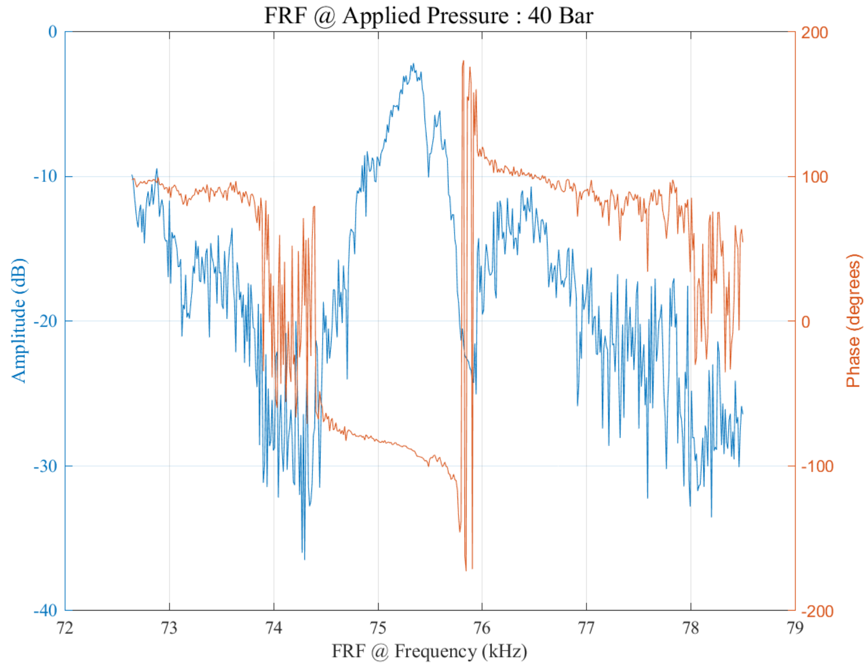

Figure 5.19 - Frequency response of the device at 40 Bars of applied pressure

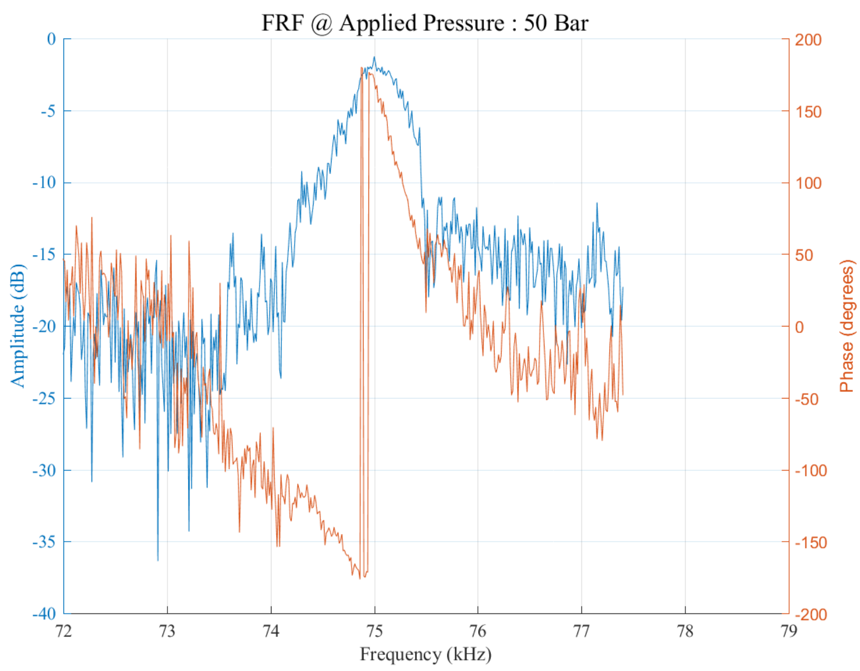

Figure 5. 20 - Frequency response of the device at 50 Bars of applied pressure

In pressure tests 884 Hz frequency shift is observed for 50 Bars of hydraulic pressure application which corresponds to a 17.68 Hz/Bar pressure sensitivity on average. As expected minimum and maximum sensitivity is obtained between 0-10 Bars and 40-50 Bars with corresponding values of 5 Hz/Bar and 34.40 Hz/Bar, respectively. The tabulated results are given in Figure 5.1.

Table 5.1 - Natural frequencies extracted from Figure 5.15 - 20 by curve fitting

Pressure	Natural Frequency
0 Bars	75928.2 kHz
10 Bars	75794.0 kHz
20 Bars	75845.3 kHz
30 Bars	75652.2 kHz
40 Bars	75355.0 kHz
50 Bars	75021.7 kHz

Remember that displacement tests suggested a value of 9.45 Hz/Bar for maximum sensitivity. The difference is mainly because the displacement test equipment along with the sensor itself cannot be fixed completely. As piezoelectric actuator pushes sensor, both of them moves a little, hence sensitivity is measured inaccurately. However the sensor is fixed well inside the device and hence the sensitivity is measured more accurately.

As mentioned before noise affected response is also expected. This can be eliminated by improving the design for higher quality factor and output voltage.

Finally, hydraulic pressure vs natural frequency curve is shown the following figure,

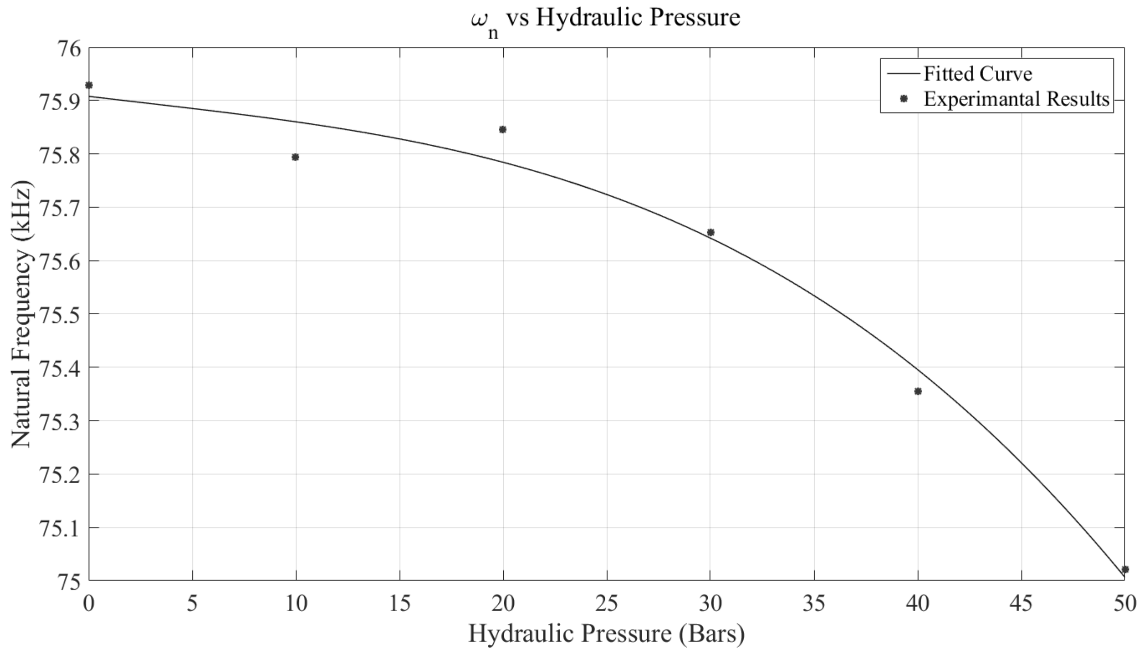

Figure 5.21 - Natural frequency vs hydraulic pressure data given with 3rd order polynomial fit.

The curve shown in Figure 5.21 is the 3rd order polynomial fit for the experimental data. The equation for this curve is as follows,

$$\omega_n = -6.36\times10^{-3}x^3 + 5.05\times10^{-2}x^2 - 4.65x + 75907.87 \qquad (5.1)$$

For the collected data the largest absolute error for this curve is 66 Hz. It is a very large error and most probably due to a measurement error.

5.6. *Summary*

Test results of the devices which have the optimized geometry are demonstrated. Along with these results, detection setup and assembly of the sensor with pressure port is described. Tests are performed in three types. First the working devices are determined and separated with resonance tests. The resonance tests are conducted with probe station without taking electrical connections by means of wiring. Secondly, displacement tests are performed with working devices by using a precise piezoelectric actuator.

Approximately 120 μm of deflection is simulated in these tests and corresponding results are plotted. As an outcome, expected frequency shift is demonstrated. In the third phase of tests MEMS sensor is assembled with pressure port in order to sense the center deflection of the diaphragm under application of hydraulic pressure. Frequency response of the assembled device at 6 different data points between 0 and 50 bars is presented. Finally applied hydraulic pressure is related with natural frequency by a fitted curve and its expression is given.

CHAPTER 6

FUTURE REMARKS AND DISCUSSIONS

Design optimization and operation of a MEMS based resonant hydraulic pressure sensor is presented. Dissertation proposes a novel method for measuring pressure with tuning fork resonator which may promote superior sensing properties in the future. For the time being it is successfully demonstrated that a very sensitive tuning fork tip can be utilized in orthogonal direction to diaphragm.

Although the sensitivity of the device is not as high as its counterparts yet, this can be enhanced greatly in the future. Spring element with a greater stiffness can be used. Then the tip of the device would deflect more under unit pressure. Before assembly of device, 100 µm deflection capability was assumed to suffice, however, it seems that it is more than enough. The tip does not get broken under the effect of sensor's own mass. Even the added mass of circuit board is acceptable. That's why, sensor can be placed into the cylinder of pressure port easily in vertical configuration. The only condition for that is to have a precisely machined diaphragm surface which is also achievable with better machining equipment. As a result of this modification, sensitivity of the device can be multiplied by 100 times.

As a future study, analytical model of the structure can be modified to govern 2 masses which is more appropriate for longer capacitive plates. This model would give more accurate results, since it can include the stiffness of the plates.

Also temperature compensation should be added to the device because it is seen during tests, temperature of the hydraulic pressure setup gets increases quite a bit. Knowing that silicon has a temperature coefficient of Young's Modulus as -60 ppm/K [36] the resonance frequency shifts with temperature only which could cause misinterpretation of sensed domain.

Natural frequency of the device was very different than single degree of freedom model. But this was expected because of long capacitive plates which are assumed to be rigid. The natural frequency of the device was found as 79.48 kHz after addition of spring and roller structure. However, microfabricated devices has a natural frequency around 71.5 kHz. This can be explained by residual stresses which may already present in the wafer and undercut. It makes sense that residual stress is effective because the operation principle of sensor relies back to application of loading, which causes stress, which causes frequency change. Moreover undercut in fabrication steps decreases the stiffness more than it decreases mass, because length of the tines stays constant while the width decreases. As a consequence, natural frequency is deviated from expected by 10 %. But this changed the expectation for other properties such as quality factor as well. For example FEM model finds width of one tine as 14.7 μm for the optimized design dimensions to have a natural frequency of 71.5 kHz. When this value is inserted into analytical model for estimating quality factor, the resultant quality factor is obtained as 273. Remembering that optimization routine finds quality factor as 339 without the effects of undercut, quality factor estimation of 273 is 15 % closer to measured value with 14 % accuracy.

In the literature quality factors of 1800 are reached with DETF resonators which have comb fingers [20]. The sensitivity of an optical MEMS hydraulic pressure sensor which has 200 bars measurement range is reported in the literature with a sensitivity of 13.17 Hz/Bar [10]. For a narrower range of 4 bars 2014 Hz/Bar of sensitivity is also present [20]. For the proposed sensor, sensitivity and quality factor is subject to increase after few modifications on the geometry. First of all, removing spring element from the structure could increase the sensitivity 100 times which is left as a future work. Also diaphragm which is machined with proper equipment to have optimum thickness would multiply the sensitivity by 1.5. Therefore 17.68 Hz/Bar sensitivity promise a lot for the future. Moreover with a slight modification on the comb finger length quality factor of the devices can be boosted up to 2500 in theory.

Fabrication has to be developed a lot in this process too. But very simple and helpful suggestion on fabrication is that the 4th photolithography mask can be used as the 1st, i.e. fabrication could have started with handle layer oxide patterning and continue from the 1st mask. This is mainly because burden and difficulty of patterning the backside while the device layer silicon is patterned and etched. On the other hand if the process starts with the 4th mask, then there is no need for binding any wafer to SOI.

Another point which is missing in the design was tip protection. Devices have very vulnerable tips which can be damaged in the slightest mistake. A capping layer of wafer would be very effective for protecting the tip from accidental out of plane loads, but at least tip could have been buried into device leaving only 100 µm at the outside for deflection. During tests, this would have prevented at least 50 % percent of accidents which resulted in device loss.

As a remaining study, self-resonance circuitry with feedthrough cancellation may be applied to devices. Without feedthrough cancellation, since the quality factor is low, stray capacitances cannot be dominated by resonance peak well. Therefore when applied both, resonance can be sustained. This would also pave the way for measuring resolution of the sensor.

REFERENCES

[1] K. E. Petersen, "Silicon as a mechanical material," *Proceedings of the IEEE*, vol. 70, pp. 420-457, 1982.

[2] G.-C. Manuel and H. Vlad, "Using a Torsional Balance to Characterize Thrust at Micro Newton Levels," in *39th AIAA/ASME/SAE/ASEE Joint Propulsion Conference and Exhibit*, ed: American Institute of Aeronautics and Astronautics, 2003.

[3] K. Bongsang, R. N. Candler, M. Hopcroft, M. Agarwal, P. Woo-Tae, and T. W. Kenny, "Frequency stability of wafer-scale encapsulated MEMS resonators," in *Solid-State Sensors, Actuators and Microsystems, 2005. Digest of Technical Papers. TRANSDUCERS '05. The 13th International Conference on*, 2005, pp. 1965-1968 Vol. 2.

[4] M. Strano, "Optimization under uncertainty of sheet-metal-forming processes by the finite element method," *Proceedings of the Institution of Mechanical Engineers, Part B: Journal of Engineering Manufacture*, vol. 220, pp. 1305-1315, 2006.

[5] P. Ray and B. J. Mac Donald, "Determination of the optimal load path for tube hydroforming processes using a fuzzy load control algorithm and finite element analysis," *Finite Elements in Analysis and Design*, vol. 41, pp. 173-192, 11// 2004.

[6] J. Paros, E. Bernard, J. Delaney, C. Meinig, M. Spillane, P. Migliacio, *et al.*, "Breakthrough underwater technology holds promise for improved local tsunami warnings," in *Underwater Technology (UT), 2011 IEEE Symposium on and 2011 Workshop on Scientific Use of Submarine Cables and Related Technologies (SSC)*, 2011, pp. 1-9.

[7] H. Matsumoto, E. Araki, and K. Kawaguchi, "Initial characteristics of pressure sensors," in *Underwater Technology (UT), 2015 IEEE*, 2015, pp. 1-5.

[8] A. J. Trujillo, B. Guamis, and C. Carretero, "A procedure for the manufacture of goat milk cheese with controlled-microflora by means of high hydrostatic pressure," *Food Chemistry,* vol. 69, pp. 73-79, 4// 2000.

[9] X. Ma, "Research on the best autofrettage pressure of ultra-high pressure valve body," in *Key Engineering Materials* vol. 667, ed, 2016, pp. 524-529.

[10] W. Challener, S. Palit, R. Jones, L. Airey, R. Craddock, and A. Knobloch, "MOEMS pressure sensors for geothermal well monitoring," 2013, pp. 861603-861603-12.

[11] G. Fragiacomo, K. Reck, L. Lorenzen, and E. Thomsen, "Novel Designs for Application Specific MEMS Pressure Sensors," *Sensors,* vol. 10, p. 9541, 2010.

[12] H. I. Kuo and W. H. Ko, "Smart-cut™ piezoresistive strain sensors for high temperature applications," in *Proceedings of IEEE Sensors*, 2009, pp. 1290-1292.

[13] M. Rajavelu, D. Sivakumar, J. Daniel Rathnam, and K. Sumangala, "Enhanced sensitivity with extended linearity in MEMS piezoresistive pressure sensor," *Micro and Nano Letters,* vol. 8, pp. 753-756, 2013.

[14] P. K. Kinnell and R. Craddock, "Advances in Silicon Resonant Pressure Transducers," *Procedia Chemistry,* vol. 1, pp. 104-107, 9// 2009.

[15] Z. Dibi, A. Boukabache, and P. Pons, "Combined effect of the membrane flatness defect and real dimensions gauges on the sensitivity of a silicon piezoresistive pressure sensor," in *Proceedings of IEEE Sensors*, 2002, pp. 990-993.

[16] A. Cheshmehdoost and B. E. Jones, "Design and performance characteristics of an integrated high-capacity DETF-based force sensor," *Sensors and Actuators A: Physical,* vol. 52, pp. 99-102, 3// 1996.

[17] K. Petersen, F. Pourahmadi, J. Brown, P. Parsons, M. Skinner, and J. Tudor, "Resonant beam pressure sensor fabricated with silicon fusion bonding," in *Solid-State Sensors and Actuators, 1991. Digest of Technical Papers, TRANSDUCERS '91., 1991 International Conference on*, 1991, pp. 664-667.

[18] K. Azgin and L. Valdevit, "The effects of tine coupling and geometrical imperfections on the response of DETF resonators," *Journal of Micromechanics and Microengineering,* vol. 23, p. 125011, 2013.

[19] M. A. Schmidt and R. T. Howe, "Silicon Resonant Microsensors," in *14th Automotive Materials Conference: Ceramic Engineering and Science Proceedings*, ed: John Wiley & Sons, Inc., 2008, pp. 1019-1034.

[20] S. Ren, W. Yuan, D. Qiao, J. Deng, and X. Sun, "A Micromachined Pressure Sensor with Integrated Resonator Operating at Atmospheric Pressure," *Sensors,* vol. 13, p. 17006, 2013.

[21] C. J. Welham, J. Greenwood, and M. M. Bertioli, "A high accuracy resonant pressure sensor by fusion bonding and trench etching," *Sensors and Actuators A: Physical,* vol. 76, pp. 298-304, 8/30/ 1999.

[22] D. Chen, Y. Li, M. Liu, and J. Wang, "Design and experiment of a laterally driven micromachined resonant pressure sensor for barometers," *Procedia Engineering,* vol. 5, pp. 1490-1493, // 2010.

[23] B. Xie, Y. Xing, Y. Wang, J. Chen, D. Chen, and J. Wang, "A Lateral Differential Resonant Pressure Microsensor Based on SOI-Glass Wafer-Level Vacuum Packaging," *Sensors,* vol. 15, p. 24257, 2015.

[24] M. H. Houston and J. M. Paros, "High accuracy pressure instrumentation for underwater applications," in *Underwater Technology, 1998. Proceedings of the 1998 International Symposium on*, 1998, pp. 307-311.

[25] X. Zhou, T. Jiang, J. Zhang, X. Wang, and Z. Zhu, "Humidity sensor based on quartz tuning fork coated with sol–gel-derived nanocrystalline zinc oxide thin film," *Sensors and Actuators B: Chemical,* vol. 123, pp. 299-305, 4/10/ 2007.

[26] R. G. Hennessy, M. M. Shulaker, M. Messana, A. B. Graham, N. Klejwa, J. Provine, *et al.*, "Vacuum encapsulated resonators for humidity measurement," *Sensors and Actuators B: Chemical,* vol. 185, pp. 575-581, 8// 2013.

[27] P. Thiruvenkatanathan, J. Yan, and A. A. Seshia, "Ultrasensitive mode-localized micromechanical electrometer," in *Frequency Control Symposium (FCS), 2010 IEEE International*, 2010, pp. 91-96.

[28] E. J. Ng, L. Hyung Kyu, C. H. Ahn, R. Melamud, and T. W. Kenny, "Stability measurements of silicon MEMS resonant thermometers," in *Sensors, 2011 IEEE*, 2011, pp. 1257-1260.

[29] D. R. Myers and A. P. Pisano, "Torque measurements of an automotive halfshaft utilizing a MEMS resonant strain gauge," in *TRANSDUCERS 2009 - 15th International Conference on Solid-State Sensors, Actuators and Microsystems*, 2009, pp. 1726-1729.

[30] M. W. Chan, D. R. Myers, B. D. Sosnowchik, L. Lin, and A. P. Pisano, "Localized strain sensing using high spatial resolution, highly-sensitive MEMS resonant strain gauges for failure prevention," in *2011 16th International Solid-State Sensors, Actuators and Microsystems Conference, TRANSDUCERS'11*, 2011, pp. 2859-2862.

[31] S. X. P. Su, H. S. Yang, and A. M. Agogino, "A resonant accelerometer with two-stage microleverage mechanisms fabricated by SOI-MEMS technology," *Sensors Journal, IEEE,* vol. 5, pp. 1214-1223, 2005.

[32] X. Zou, P. Thiruvenkatanathan, and A. A. Seshia, "A high-resolution micro-electro-mechanical resonant tilt sensor," *Sensors and Actuators, A: Physical,* vol. 220, pp. 168-177, 2014.

[33] W. Zhang and J. E. Y. Lee, "Frequency-based magnetic field sensing using Lorentz force axial strain modulation in a double-ended tuning fork," *Sensors and Actuators A: Physical,* vol. 211, pp. 145-152, 5/1/ 2014.

[34] K. Azgin, T. Akin, and L. Valdevit, "Ultrahigh-dynamic-range resonant MEMS load cells for micromechanical test frames," *Journal of Microelectromechanical Systems,* vol. 21, pp. 1519-1529, 2012.

[35] S. Fan, L. Wang, and Z. Guo, "A novel micro-electromechanical resonant gyroscope," 2008, pp. 71270D-71270D-7.

[36] M. A. Hopcroft, W. D. Nix, and T. W. Kenny, "What is the Young's Modulus of Silicon?," *Microelectromechanical Systems, Journal of,* vol. 19, pp. 229-238, 2010.

[37] W. Wang, J. Jia, and J. Li, "Slide film damping in microelectromechanical system devices," *Proceedings of the Institution of Mechanical Engineers, Part N: Journal of Nanoengineering and Nanosystems,* vol. 227, pp. 162-170, 2013.

[38] Z. Xia and W. C. Tang, "Viscous air damping in laterally driven microresonators," in *Micro Electro Mechanical Systems, 1994, MEMS '94, Proceedings, IEEE Workshop on*, 1994, pp. 199-204.

[39] A. Torrents, K. Azgin, S. W. Godfrey, E. S. Topalli, T. Akin, and L. Valdevit, "MEMS resonant load cells for micro-mechanical test frames: feasibility study and optimal design," *Journal of Micromechanics and Microengineering*, vol. 20, p. 125004, 2010.

[40] S. Timoshenko and S. Woinowsky-Krieger, *Theory of plates and shells*: McGraw-Hill, 1959.